Mesoarchaean (2820 Ma) high-pressure mafic granulite at Uauá, São Francisco Craton, Brazil, and its potential significance for the assembly of Archaean supercratons

Mesoarchaean (2820 Ma) high-pressure mafic granulite at Uauá, São Francisco Craton, Brazil, and its potential significance for the assembly of Archaean supercratons

Elson P. Oliveira[1*], Cristina Talavera[2#], Brian F. Windley[3], Lei Zhao[4], Julia J. Semprich[5], Neal J. McNaughton[2], Wagner S. Amaral[1], Gabriel Sombini[1], Margareth Navarro[1], Dailto Silva[1]

[1]Department of Geology and Natural Resources, Institute of Geosciences, University of Campinas, 13083-970 Campinas, Brazil

[2]John de Laeter Centre, Curtin University, Perth, WA 6845, Australia

[3]Department of Geology, The University of Leicester, Leicester LE1 7RH, United Kingdom

[4]Institute of Geology, Chinese Academy of Geological Sciences, Beijing, 100037, China

[5]Lunar and Planetary Institute, Universities Space Research Association, Houston 77058, USA

---

* Corresponding author at: Department of Geology and Natural Resources, Institute of Geosciences, University of Campinas, 13083-970 Campinas, Brazil.
Phone: +55-1935215158; E-mail address: elson@ige.unicamp.br

Current address: School of Geosciences, University of Edinburgh, The King's Buildings, James Hutton Road, Edinburgh EH9 3FE, UK.

Abstract

High pressure (HP) granulites of regional scale form as a result of tectonic events that lead to crustal thickening or subduction of the crust into the mantle. Most HP granulites are Phanerozoic, a few are Proterozoic, and Archaean HP granulites are even scarcer. Here we present field relationships, mineral chemistry and zircon U-Pb ages, Hf isotope data and trace elements data for the mafic granulite and associated rocks of the Uauá terrane, São Francisco Craton, Brazil, as evidence for the likely existence of a thick continental crust in the Mesoarchaean/Neoarchaean transition. The HP mafic granulite occurs as lensoid bodies within shallow dipping diorite to leucodiorite gneisses. Small scale layering between mafic granulite and diorite gneiss indicate these rocks are cogenetic. Garnet-clinopyroxene pairs with quartz, zircon, ilmenite, plagioclase, and clinopyroxene inclusions in garnet characterize the HP assemblage. Garnet porphyroblasts also show opx-cpx-plag symplectite coronas, which coupled with hornblende and plagioclase define PT conditions to lower grade granulite and amphibolite facies. Microprobe data combined with phase equilibria modelling (pseudosections) indicate 16-18 kbar and 930-960 °C for the peak HP assemblage, and 6.2-7.0 kbar and 660-760°C for lower pressure granulite to amphibolite facies symplectite coronas. Metamorphic zircon rims in equilibrium with garnet have SHRIMP ages of 2819 ± 14, and igneous zircon cores of 3127 ± 14 Ma. The cores of zircon in associated gneiss samples have U-Pb ages between 3090 ± 13 Ma (LA-ICP-MS) and 3125 ± 15 Ma (SHRIMP) with age cluster at 3120 ± 6 Ma. $\varepsilon_{Hf(t)}$ values on igneous zircon of the HP mafic granulite are slightly positive whereas metamorphic zircon rims are negative. The associated diorite gneiss invariably yielded negative zircon $\varepsilon_{Hf(t)}$ values. Trondhjemite sheets intrusive in the mafic granulite are ca. 20 m.y. younger (2794 ± 13 Ma) than the host granulite. We interpret the igneous protoliths of the mafic granulite and leucodiorite gneiss as a single igneous complex emplaced in the

continental crust, later deformed and metamorphosed by contraction and crustal thickening during collision of blocks/cratons to form Earth's first supercratons by the end of the Mesoarchaean.

Keywords: Archaean High-Pressure Mafic Granulite, Thermobarometry, Pseudosections, U-Pb Zircon Geochronology, Tectonics, São Francisco Craton

1. Introduction

Most exposed Archaean crust is composed of low-grade granite-greenstone terranes and high-grade granulite-gneiss terranes (e.g. Windley 1995; Condie 2011). Whereas the low-grade terranes have been well studied (e.g. Polat al., 2009; Dilek and Furnes 2014), the high-grade metamorphic terranes are less well known, because of their more intense deformation and metamorphism, and because of the scarcity of modern analogues/equivalents (Windley and Garde, 2009). Today, most high-grade terranes have an amphibolite or granulite facies metamorphic grade, many amphibolite facies terranes retain evidence of retrogression from the granulite facies, and many have undergone major imbricate thrusting and tectonic intercalation, followed by several phases of isoclinal to tight folding and granulite-amphibolite facies metamorphism (e.g. Myers, 1976; Sajeev and Santosh, 2006). Thus, deep crustal sections of orogenic bels are still poorly understood compared with upper crustal sections (Polat et al., 2009; Dumond et al., 2010; Dilek and Furnes, 2014).

High-pressure (HP) granulites occur as layers and lenses in high-grade granulite-gneiss terranes; they form as a result of crustal thickening by collision (Brown, 2009), subduction of the crust into the mantle (O'Brien and Rötzler, 2003), or cooling from magmatic conditions to HP metamorphic conditions at the base of island arc complexes (De Paoli et al., 2009; Brown, 2009). The minimum PT conditions for HP granulite

78 formation range from 11.5 kbar and 680°C (Oh and Liou, 1988) to 9 kbar and 620°C
79 (Sajeev and Santosh, 2006). Most HP granulites are Phanerozoic, there are fewer well-
80 documented occurrences of early to late Proterozoic age (Baldwin et al., 2006), and
81 Archaean HP granulites are even scarcer. The aim of this paper is to report a new
82 discovery of ca. 2.8 Ga HP mafic granulites in the Uauá terrane, São Francisco Craton,
83 Brazil, in order to provide much needed information on the make-up and evolution of
84 the lower crust of orogenic belts.
85
86 **2. Geological Setting**
87 The São Francisco Craton (SFC) in eastern Brazil (Fig. 1) is surrounded by
88 Neoproterozoic orogens (Araçuaí, Brasília, Riacho do Pontal, Rio Preto, and
89 Sergipano).
90 The basement rocks of the SFC are dominated by Archaean to Palaeoproterozoic
91 migmatites, amphibolite to granulite-grade gneisses, and granite-greenstones (Teixeira
92 et al., 2017). Meso-Neoproterozoic sedimentary rocks of the Espinhaço and São
93 Francisco Supergroups cover those rocks. The SFC, which aggregated during the
94 Archaean and Proterozoic mainly in the interval 2.1-1.8 Ga, is made up of several
95 greenstone belts (e.g. the Rio Capim, Rio Itapicuru, Mundo Novo, Umburanas, and Rio
96 das Velhas) and microcontinental blocks (e.g. the Gavião, Jequié, Itabuna-Salvador-
97 Curaçá orogen and Serrinha). Relevant here is the Serrinha Block, which contains the
98 Uauá high-pressure mafic granulites.
99
100
101
102
103

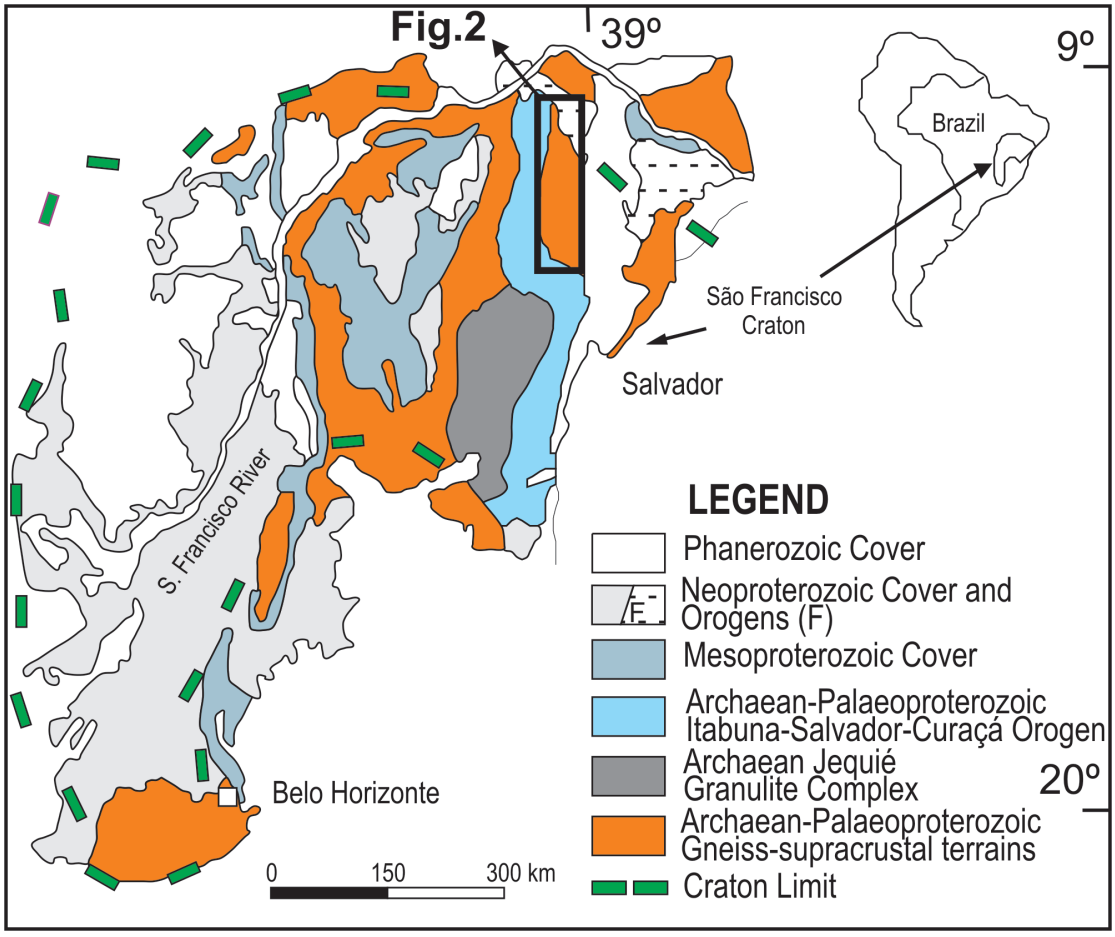

Fig. 1. The main geologic units of the São Francisco Craton (modified from Oliveira et al., 2004). The box indicates the Serrinha Block that contains the Uauá high-pressure mafic granulite.

The Serrinha Block, or microcontinent (Fig. 2a) is composed of amphibolite to granulite facies grey gneisses of the Tonalite-Trondhjemite-Granodiorite (TTG) suites, migmatitic grey gneisses, banded gneisses, marbles, BIFs, mafic dykes and mafic-ultramafic complexes; the banded gneisses are the end-products of deformation of the migmatitic TTG gneisses and mafic dykes (Oliveira et al., 2010). These rocks are in tectonic contact with the supracrustal Palaeoproterozoic Rio Itapicuru and Rio Capim greenstone-granite belts. The grey gneisses have ages from 3151 Ma to 2933 Ma and crop out continuously close to the towns of Retirolândia and Uauá, and along the

Jacurici river (R, U and J, respectively in Fig. 2a); they may be terranes of the Serrinha Block (Oliveira et al., 2010). The Rio Itapicuru low-grade supracrustal greenstone belt (RIGB in Fig. 2a) is about 180 km long, 30 km wide and has three lithostratigraphic subdivisions: (i) a basal mafic volcanic unit composed of massive and pillowed basaltic flows intercalated with chert, banded iron-formation, and carbonaceous shale; (ii) an intermediate to felsic volcanic unit with meta-dacites, meta-andesites and meta-pyroclastic rocks, and (iii) a meta-sedimentary pelitic-psammitic unit mainly composed of meta-pelites and minor chemical sedimentary rocks. Zircon and xenotime U-Pb geochronological data indicate this belt formed between 2170 Ma and 2080 Ma (Mello et al., 2006, Oliveira et al., 2010). The high-pressure mafic granulite occur in the Uauá terrane, which is bounded by the Rio Capim greenstone belt and the Caldeirão shear belt, the geological details of which are given below.

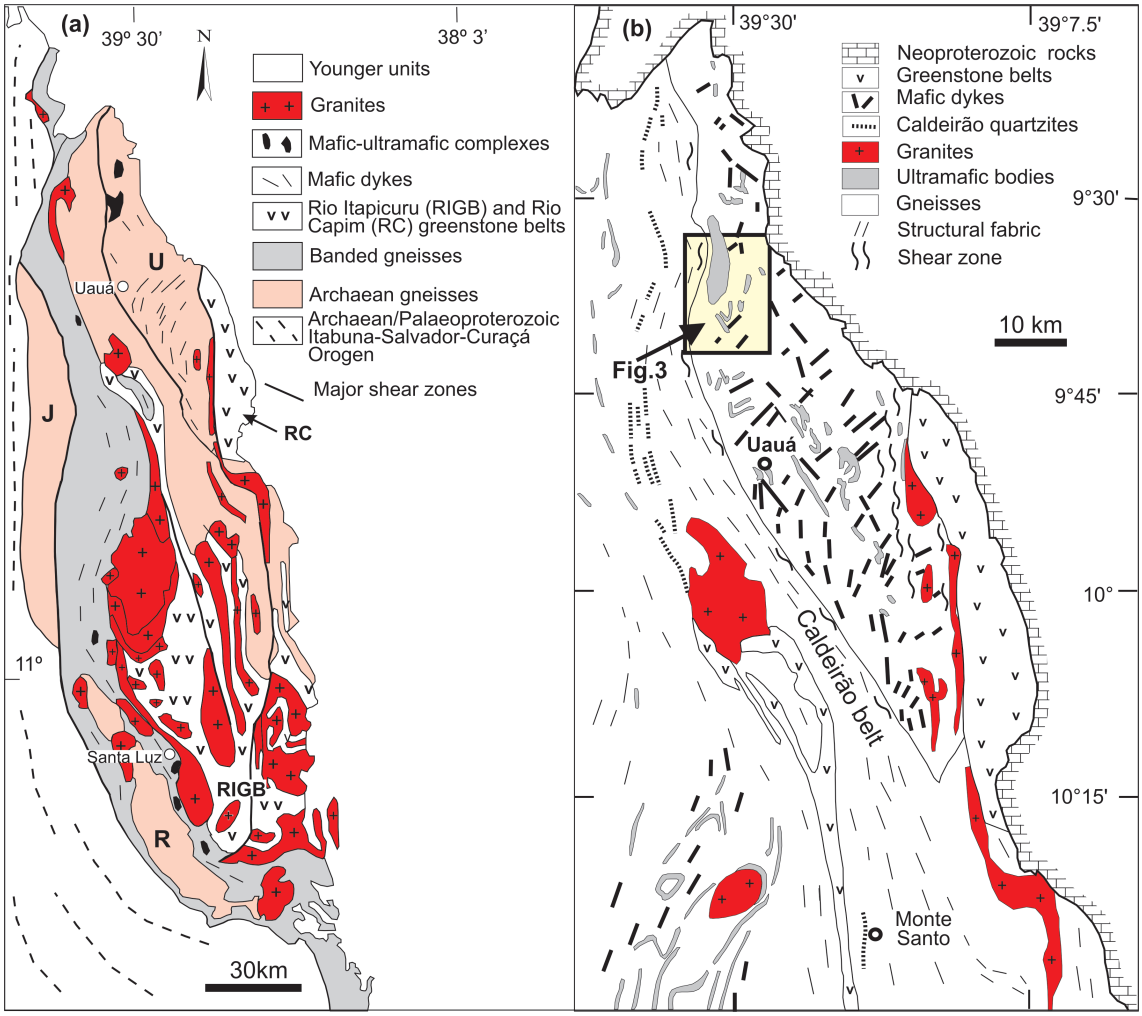

Fig. 2. The Serrinha Block and its main geological units. a) Letters show the Mesoarchaean grey gneisses, or terranes of Retirolândia (R), Jacurici (J), and Uauá (U). The banded gneisses (in gray) are the metamorphic product of collision between the Mesoarchaean terranes and the Palaeoproteozoic greenstone belts (RIGB and RC); after Oliveira et al. (2010). b) Detail of the Uauá terrane bounded by shear zones with the Caldeirão belt (west) and the Rio Capim greenstone belt (east). Fig. 3 shows location of the high-pressure mafic granulite.

2.1. The Uauá Terrane

The Uauá terrane (Fig. 2b; Uauá pronounced like the Canadian town "Wawa") was displaced from south to north (present-day coordinates) during Palaeoproterozoic oblique collision (Oliveira et al., 2004; Oliveira et al., 2010, Oliveira, 2011). It is bordered to the west by the Archaean-Palaeoproterozoic Caldeirão shear belt and to the east by the Palaeoproterozoic Rio Capim greenstone belt. Neoproterozoic continental shelf metasedimentary rocks of the Sergipano orogen cover all these units.

The Uauá terrane consists mostly of NW-trending banded gneisses of unknown age, layered anorthosite-peridotite-diorite complexes, and tonalite-granodiorite bodies (Oliveira, 2011), most of which were metamorphosed under granulite facies conditions and later retrogressed to amphibolite grade. Mesoarchaean ages are widespread in the Uauá terrane. Anorthosites of the Lagoa da Vaca layered anorthosite complex have a 3161 ± 65 Ma whole-rock Pb-Pb isochron, and orthogranulites have a zircon Pb-evaporation age of 3072 ± 20 Ma (Paixão and Oliveira, 1998). Granulite and a gneissic granodiorite near Uauá town contain 2933 ± 3 Ma and 2991 ± 22 Ma zircons, respectively (Oliveira et al., 2002). The following rocks have zircon LA-ICP-MS ages: near Uauá there are ca. 2960 Ma folded sanukitoid sheets, 2955 Ma granodiorite

157 gneisses, and 3075 Ma gabbro lenses, stacked in N-verging nappes, whereas east of
158 Uauá the rocks are less deformed and mainly represented by the ca. 3098-3079 Ma calc-
159 alkaline Capim Tonalite, the 3085 Ma Caratacá porphyritic tonalite-granodiorite, and
160 grey gneisses (Oliveira et al., 2016).

161 Two mafic dyke swarms intrude the Archaean gneisses of the Uauá terrane (Fig.
162 2b); a NW-trending swarm of metamorphosed tholeiite dykes and unmetamorphosed or
163 weakly metamorphosed 2726 Ma norite-pyroxenite dykes, and a NE-trending swarm of
164 unmetamorphosed 2624 Ma tholeiite dykes (Oliveira et al., 2013). Crosscutting
165 relations and drag folds indicate the NE-trending dykes are the younger (Oliveira, 2011;
166 Oliveira et al., 2013).

167 The 10 km-wide Caldeirão shear belt (Fig. 2b) comprises steeply dipping
168 quartzites, sillimanite-cordierite-garnet gneisses, granodiorite gneisses, mafic rocks and
169 migmatites, all metamorphosed in the amphibolite facies; the granodiorite gneiss
170 protoliths have a SHRIMP U-Pb age of 3150 Ma age (Oliveira et al., 2002). To the
171 south, the shear belt is dismembered into narrow sinistral strike-slip shear zones, one of
172 which continues for over 150 km across the Rio Itapicuru greenstone belt. The
173 boundary of this shear belt to the Uauá terrane is gradational and marked by refolding of
174 older structures, by granite and pegmatite intrusions, and by shear zones. Detrital zircon
175 grains in quartzites and syn-deformational titanite in mafic dykes constrain the quartzite
176 protolith depositional age to a maximum of 2700 Ma and a regional metamorphic age to
177 between 2039 and 2077 Ma (Oliveira et al., 2000, 2002).

178 The Rio Capim greenstone belt (Fig. 2) is a 10-km wide, 80-km long, N/NW-
179 trending belt of deformed and metamorphosed mafic to felsic volcanic and associated
180 pelitic rocks, intruded by plutons ranging in composition from gabbro/diorite to granite
181 (Oliveira et al., 2011). In this belt the metamorphic grade increases from greenschist
182 facies in the west to granulite in the east. Zircon U-Pb ages of the felsic volcanic, diorite

and granite fall in the range 2148-2128 Ma (Oliveira et al., 2011). The contact of the Rio Capim greenstone belt and the Uauá terrane is occupied by the 20-500 meter-wide, NS-trending, upright Galo do Ouro dextral shear zone (Oliveira, 2011).

2.1.1. The mafic granulite containing HP relics

The mafic granulite occurs as dozen to hundred m-wide and several hundred m- to km-long lensoid bodies within quartz diorite, leucodiorite to granodiorite gneisses (Fig. 3). The black arrow in Fig. 3 indicates the largest and most continuous outcrop of mafic granulite containing high-pressure relics, which forms a swarm of narrow massive to layered bands (Fig. 4a), massive lenses with disseminated garnet (Fig. 4b), garnet-rich pods (Fig. 4c), and garnet-rich boudins (Fig. 4d) within mafic granulite partially retrogressed to amphibolite facies. The contact between mafic granulite and leucodiorite gneiss is gradational (Fig. 5a) suggesting that their protoliths were parts of layered complexes. Narrow trondhjemite sheets intrude the mafic granulite as evidenced by their contact paralleling (Fig. 5b) or crosscutting (Fig 5c) the host mafic granulite foliation. The associated leucodiorite/diorite gneisses dip shallowly eastwards and have a mineral stretching lineation that plunges shallowly to E-NE (Fig. 3). Locally, bands of leucodiorite gneiss are displaced along flat-ramp thrust faults indicating late contraction towards the W-SW (Fg. 5d). To the west both mafic granulite and host leucodiorite gneiss are in contact with a large body of magnetite-rich, quartz-poor, tonalite granulite, which in turn is in contact to the west with the ca. 3.16 Ga Lagoa da Vaca layered anorthosite (Paixão and Oliveira, 1998). To the east, the leucodiorite-granodiorite gneiss is intruded by granites and to the south it is tectonically imbricated with grey gneisses (Fig. 3).

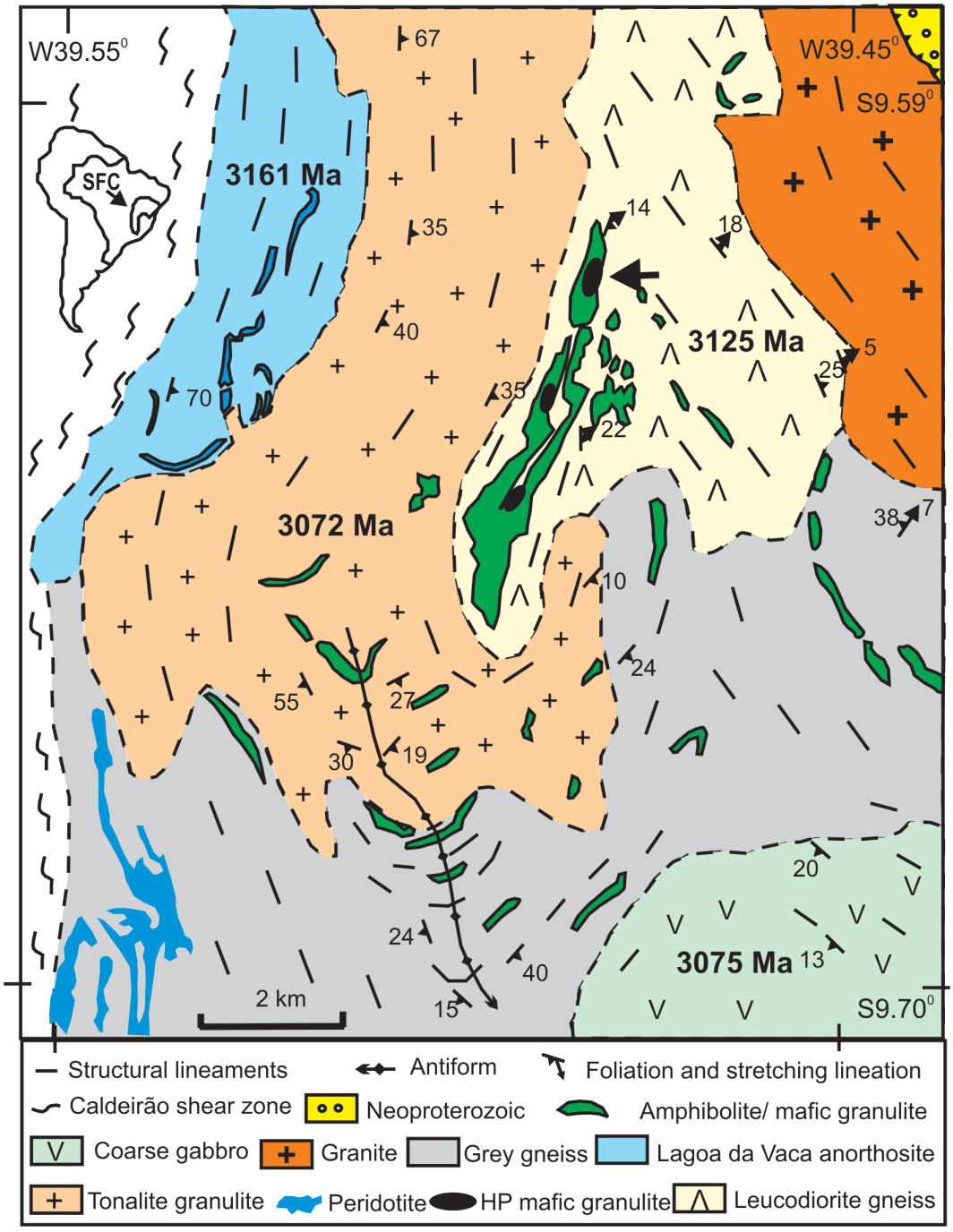

208

209 **Fig. 3.** Geological map with the main occurrences of mafic granulite. Ages of rock

210 units are from Paixão and Oliveira (1998), Oliveira et al. (2016) and this work.

211 Black arrow indicates the largest outcrop of mafic granulite where the samples for

212 this study were collected (e.g. EO182).

213

214 **Fig. 4.** Field features of the mafic granulite. a) Massive to layered mafic granulite; b)
215 disseminated garnet in mafic granulite; c) garnet-rich mafic granulite within
216 retrogressed amphibole-bearing mafic granulite; d) layers and boudin of garnet-rich
217 mafic granulite within more felsic, foliated retrogressed amphibole-bearing mafic
218 granulite. 15 cm pen and 25 mm coin for scale.

219

220

221 **Fig. 5.** Field relationships of the mafic granulite and associated leucodiorite-
222 granodiorite gneiss. a) Gradational/layered contact between mafic granulite
223 (towards figure top) and leucodiorite gneiss (towards figure bottom) suggesting
224 that the protoliths of both mafic granulite and leucodiorite gneiss were cogenetic
225 igneous rocks; b) younger trondhjemite sheets (white arrows) intrusive along the
226 mafic granulite foliation; c) narrow trondhjemite offshoot (white arrow) crosscuts
227 the mafic granulite foliation; d) shallow-dipping diorite/leucodiorite gneiss with
228 thrust fault immediately above white arrow indicating top-to-SW thrusting and
229 crustal thickening. Hammer, notebook or 15 cm pen for scale.

230

231 ***2.1.2. Petrography of the mafic granulite***

232

233 The mafic granulite shows granoblastic textures and medium-to coarse grain size. It is
234 composed of clinopyroxene, plagioclase and minor ilmenite and quartz (Fig. 6a).
235 Clinopyroxene occurs as aggregates with grains up to 1 mm and is diopsitic/augitic with
236 XMg~ 0.6 and low amounts of Na (0.02-0.03 a.p.f.u.) and Al (0.08-0.11 a.p.f.u.).

Associated plagioclase is nearly 1 mm long and andesine to labradorite in composition (An 40-60). The high-pressure granulite facies assemblage is characterized by garnet and clinopyroxene (Fig. 6b), less often plagioclase, ilmenite and quartz. Garnet porphyroblasts (up to cm size) are Fe-rich (Alm60) and contain inclusions of clinopyroxene, quartz and plagioclase (Fig. 6c,d). Garnet profiles show decreased pyrope but increased spessartine component from core to rim (see Fig. 7 in Section 4.1). Garnet grains are surrounded by symplectites of orthopyroxene + plagioclase (Fig. 6d,e), indicating retrogression to lower pressure granulite facies conditions. The retrogression continued down to amphibolite facies conditions as indicated by minor green amphibole as part of the symplectite intergrowth (Fig. 6e) and as hornblende blades aligned along the foliation plane (Fig. 6f). Symplectitic orthopyroxene occurs in small 20-25 μm wide to lesser than 300 μm long grains around garnet and has XMg ~0.4-0.3. Symplectitic plagioclase is more calcic (An 65-73) than the groundmass ones. Opaque minerals are predominantly ilmenite and, rarely, magnetite. However, magnetite is frequent in the symplectites. Neither orthopyroxene nor hornblende are present as inclusion in garnet or in equilibrium with it and are therefore not interpreted to be part of the high-pressure assemblage.

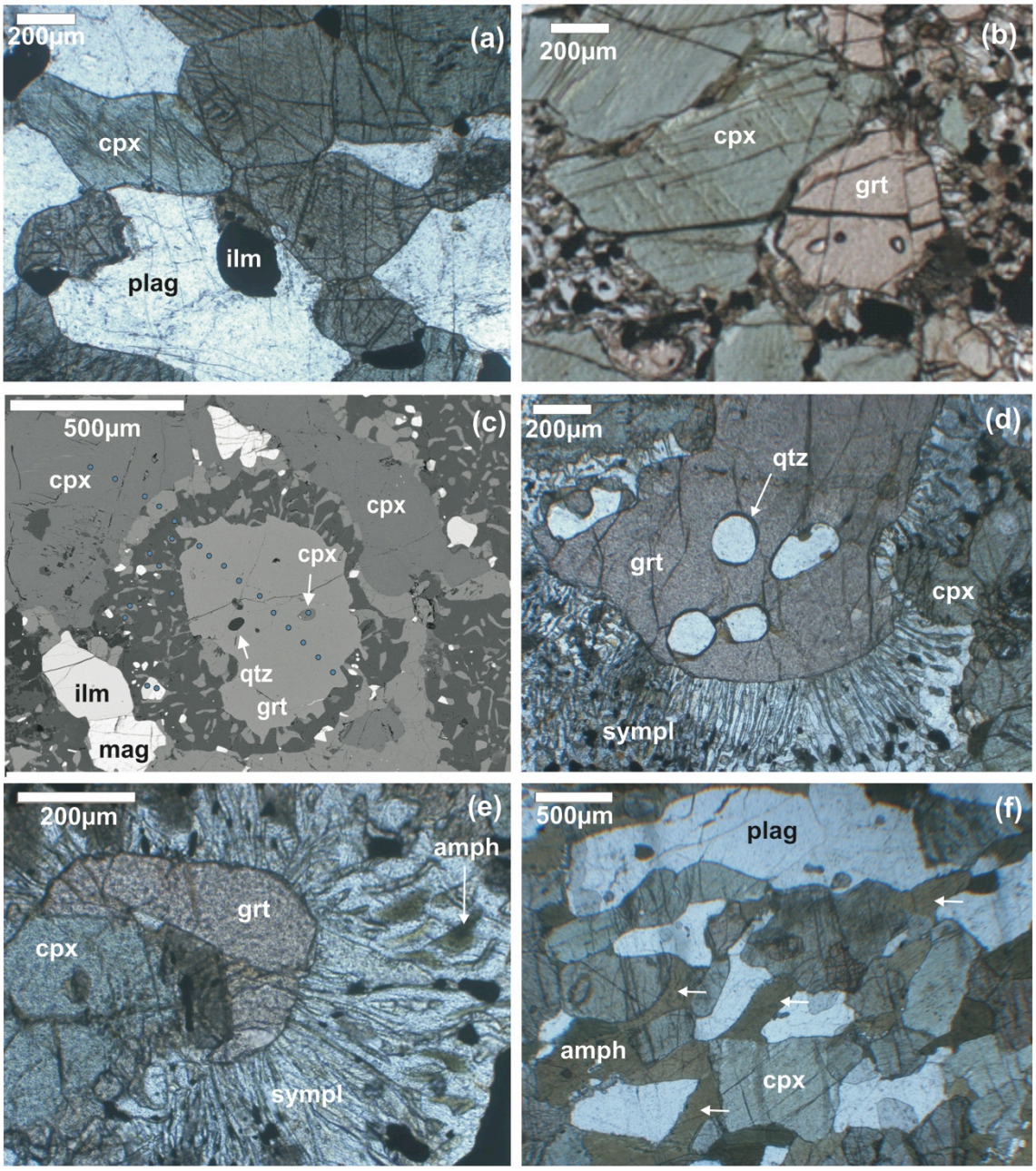

255

256 **Fig. 6.** Textures and mineralogy of the Uauá mafic granulite EO182. In all figures
257 garnet typically has a corona of opx+plag. (a) mafic granulite with clinopyroxene,
258 plagioclase and accessory ilmenite; (b) typical association of clinopyroxene and garnet
259 as the high-pressure assemblage; (c) (SEM back scatter image - BSE) garnet contains
260 cpx and quartz inclusions; (d) garnet with orthopyroxene+plagioclase sympletctites and
261 quartz inclusions; (e) Detail of garnet + clinopyroxene with opx+plag+magn+amphibole
262 symplectite - note that amphibole forms more distal to garnet in the symplectite; (f)
263 hornblende oriented along the granulite foliation. BSE bright minerals in (c) are

magnetite (white) and ilmenite (grey). In (b) garnet is in contact with cpx and in (d) garnet is separated from cpx by opx-plag symplectites. Small black circles in (c) represent electron microprobe analyses, discussed below.

3. Samples and Methods

A list of all samples used for this study with geographic coordinates is given in supplementary file Table S1.

3.1. Mineral Chemistry

Mineral analyses of sample EO182 (polished thin sections EO182a and EO182b in Table S2) were acquired for pressure-temperature calculations with a Cameca SXFive microprobe at the Federal University of Rio Grande do Sul, Brazil. The instrument operated under the following routine conditions: a) for garnet: beam current of 25 nA, beam diameter of 1 μm, and accelerating voltage of 15 kV; b) for plagioclase and pyroxenes: beam current of 15 nA, beam diameter of 1 μm, and accelerating voltage of 15 kV. The standards used were those provided commercially by SPI Supplies for microanalysis (SPI 53 minerals > http://www.2spi.com/item/02753-ab). For this paper, the following mineral standards were used for instrument calibration: jadeita (Na), almandine (Si and Fe), pyrope (Mg and Al), orthoclase (K), diopside (Ca), chromite (Cr), rodonite (Mn), rutile (Ti). The crystals used were TAP (Na, Al, Si, Mg), PET (Ca, Cr, K, Ti) and LIF (Fe, Mn).

3.2. Pressure-Temperature Quantitative Phase Diagrams (Pseudosection)

Phase equilibria modelling on a given bulk-rock composition (pseudosections) can reveal stable mineral assemblages and their evolution in P-T space, and therefore yields results independent from geothermobarometry since a priori knowledge of

290 mineral compositions is not required. We used the Gibbs free energy minimization
291 software Perple_X 6.8.6 (Connolly, 2005) and an internally consistent thermodynamic
292 data set (Holland and Powell, 2011) to calculate pseudosections in the P-T range of 5-20
293 kbar and 600-1100 °C. The whole-rock composition of sample EO182 was chosen as
294 starting composition (caption for Fig. 10) since it preserved the peak granulite-facies
295 assemblage with the lowest amount of amphibolite facies overprint. The oxides MnO
296 and P2O5 were not considered due to their relatively low abundances and/or an
297 incomplete set of solid solution models defining the compositional space as: TiO2-
298 K2O-Na2O-CaO-FeO-MgO-Al2O3-SiO2-O2 (TiKNCFMASO). The ratio of ferrous to
299 ferric iron has not been determined in the sample EO182, but based on the presence of
300 ilmenite and rare magnetite, we assume a value of 0.2 wt% O2 in the starting
301 composition, which would be similar to values constrained by the quartz-fayalite-
302 magnetite (QFM) buffer at granulite facies conditions. H2O, and consequently melting,
303 is not considered in our calculations because we are interested in the high-grade
304 granulite facies mineral assemblage, which is interpreted to be anhydrous based on
305 petrographic constraints and the negative or very small LOI values for the mafic garnet
306 granulite composition (see caption to Fig. 10). Furthermore, textural relationships in the
307 field and thin sections indicate that the mafic rocks were overprinted to amphibolite
308 facies conditions after peak granulite facies conditions. The following solid-solution
309 models were used: olivine from Holland and Powell (1998), clinopyroxene (augite)
310 from Green et al. (2016), orthopyroxene and garnet from White et al. (2014),
311 plagioclase from Holland and Powell (2003), and ilmenite-hematite from White et al.
312 (2000). Quartz, rutile and K-feldspar were assumed to be pure phases. Titanite was
313 excluded, as it has not been detected in the samples. The sum of all considered oxides is
314 normalized to 100% by Perple_X at every pressure-temperature condition.

315 In addition to the simplifications of the compositional space, extra uncertainties
316 derive from uncertainties in physical properties of end-member in the thermodynamic
317 data set, uncertainties in the formulation of activity-composition relationships,
318 analytical errors, errors in the estimation of the oxidation state, the assumption of
319 equilibrium conditions, and natural petrographic variation in the samples (e.g. Palin et
320 al., 2016). Especially the modelled stability of minor phases such as rutile and quartz
321 are sensitive to uncertainties in bulk composition and solid solution models, which is
322 why they were not considered for the determination of P-T conditions. Furthermore, the
323 ilmenite-rutile transition is sensitive to the oxidation state of the bulk rock with the
324 ilmenite stability increased towards higher pressures with increasing oxidation state.
325 Also, selected solution models do not account for small amounts of titanium, that is
326 likely present in both garnet and clinopyroxene resulting in a somewhat overestimated
327 amount of titanium-bearing oxides such as ilmenite and rutile, which also increases the
328 uncertainty.

329 **3.3. Geochronology**

330 Samples EO182, 14EW-20, 15GE-61, and a polished slab of EO182 (EO182p),
331 were selected for age dating on the SHRIMP (Table S3). Sample EO182 is a medium-
332 grained, garnet-rich granulite that is representative high-pressure mafic granulite
333 partially retrogressed to the amphibolite facies; the sample contains garnet
334 porphyroblasts, clinopyroxene, and opx+plag symplectites around garnet (as shown in
335 Fig. 6) within a groundmass of plagioclase and clinopyroxene with minor late
336 hornblende. Samples 14EW-20 and 15GE-61 are leucodiorite gneisses associated with
337 the HP mafic granulite; the two samples are mainly composed of hornblende,
338 plagioclase with minor quartz and pyroxene, the latter is often partially replaced by
339 hornblende, or hornblende + quartz.

Zircon U-Pb ages were obtained with a Sensitive High Resolution Ion Microprobe using the Perth Consortium SHRIMP II at Curtin University, Western Australia, based on the analytical procedures described by de Laeter and Kennedy (1998) and Kennedy and de Laeter (1994). Samples EO182, EO182p, 14EW-20 and 15GE-61 were analysed in three different sessions. A 25-30 μm diameter spot was used with a mass-filtered O_2^--primary beam of ~1.7-2.2 nA on zircons from samples EO182, 14EW-20 and 15GE-61, and a 10-15 μm diameter spot was used with a mass-filtered O_2^--primary beam of 1.2-1.5 nA on zircons from sample EO182p. Data for each spot was collected in sets of 6 scans on the zircons through the mass range of $^{196}Zr_2O^+$, $^{204}Pb^+$, Background, $^{206}Pb^+$, $^{207}Pb^+$, $^{208}Pb^+$, $^{238}U^+$, $^{248}ThO^+$ and $^{254}UO^+$. The $^{206}Pb/^{238}U$ age standard and U-content standard used is BR266 (559 Ma; 903 ppm U; Stern 2001). The $^{207}Pb/^{206}Pb$ standard used to monitor instrument-induced mass fractionation was OGC zircon (3467+/-3 Ma; Stern et al. 2009). The $^{207}Pb/^{206}Pb$ dates obtained on OGC zircons during the SHRIMP sessions matched the $^{207}Pb/^{206}Pb$ standard age within uncertainty and no fractionated correction was warranted. The common Pb correction was based on the measured ^{204}Pb-correction (Compston et al., 1984). The formula for Pb/U calibration is $^{206}Pb^+/^{238}U^+ = a\ (^{254}UO^+/^{238}U^+)^b$ (Claoué-Long et al., 1995) using the parameter values of Black et al. (2003). The constant "a" is determined empirically from analyses of the standard during the analytical session. The programs SQUID II and Isoplot (Ludwig 2003, 2009) were used for data processing.

Leucodiorite gneiss EO178-D was analysed by LA-ICP-MS to identify concordant grains for further Hf isotope analysis. The results are shown in Table S3. The analytical work was performed at the Institute of Geosciences, University of Campinas-UNICAMP. Isotope data were acquired on an ICP-MS Element XR (Thermo Scientific), coupled with an Excite.193 (Photon Machines) laser ablation system, equipped with a two-volume HelEx ablation cell. The acquisition protocol followed

Navarro et al. (2015) with details in Verma et al. (2016); spot size is 25 μm. Data were reduced off-line using the Iolite software (version 2.5) following the method of Paton et al. (2010), which involves subtraction of gas blank followed by downhole fractionation correction comparing with the behaviour of the 91500 reference zircon (Wiedenbeck et al., 1995). Peixe zircon standard (ID-TIMS age of 564 ± 4 Ma; cf. Dickinson and Gehrels, 2003) was used to monitor the quality of the reduction procedures; during the analytical session 14 Peixe zircon analyses yielded the average age 575 ± 10 Ma.

3.4. Trace element analyses of zircons

Rare earth element (REE) and other trace element data were obtained on dated zircons from sample EO182p (Table S4) by LA-ICP-MS at University of Campinas, in order to test for any major chemical changes in zircon during high-grade metamorphism. The REE data were acquired on an ICP-MS Element XR (Thermo Scientific), coupled with an Excite.193 (Photon Machines) laser ablation system, equipped with a two-volume HelEx ablation cell. The standard Nist612 was used for trace element calibration, and zircon standard 91500 (Wiedenbeck et al., 1995) was analysed (10 spots) as an unknown for analysis validation.

3.5. Hafnium isotope analyses of zircons

Concordant zircons from samples EO182 and EO178-D were analysed for Hafnium isotope data (Table S5) at Federal University of Ouro Preto, Brazil, using a multi-collector (MC)-ICP-MS Thermo-Scientific Neptune Plus system coupled to a Photon Machines 193 (λ = 193 nm) ArF Excimer laser ablation system, and following the analytical procedures of Albert et al. (2016). During the two analytical sessions 7 and 11 spot analyses of GJ-1 zircon ($^{176}Hf/^{177}Hf$=0.282000 ± 0.00005; Morel et al., 2008) yielded average $^{176}Hf/^{177}Hf$ ratios of 0.282005 ± 0.00020 and 0.282004 ± 0.00019, respectively.

3.6. Whole-rock geochemistry

Whole-rock geochemistry of mafic granulite EO182 (caption for Fig. 10) for phase equilibria modelling was undertaken at the University of Campinas with a Philips PW2100 X-ray fluorescence spectrometer using fusion beads for major and minor elements following the analytical procedures of Vendemiato and Enzweiler (2001).

4. Results

4.1. Metamorphic conditions: Thermobarometry

Mineral compositions of two polished thin sections of sample EO182 (EO182a and EO182b) were analysed for thermobarometry calculations. Representative mineral compositions are presented in Table S2 (supplemental files).

Garnet-clinopyroxene pairs with quartz, zircon, ilmenite, plagioclase, and clinopyroxene inclusions in garnet define the high-pressure assemblage. Garnet porphyroblasts also show opx-cpx-plag symplectite coronas, which coupled with hornblende and plagioclase, define the retrogressive conditions to lower grade granulite and amphibolite facies.

Reaction textures preserved in the mafic granulite indicate that it experienced severe retrogression after peak metamorphic stage. Chemical zoning patterns of the garnet show clear decrease of X_{Pyr} and increase of X_{Spes} from core to rim. The variations of X_{Alm} and X_{Gro} are not so obvious and they seem to remain the same from core to rim (Fig. 7; transect shown in Fig. 6c). Such chemical zoning patterns of garnet belong to typical diffusion zoning patterns usually developed during retrograde metamorphism (Spear and Selverstone, 1983; Spear et al., 1990). In such kind of rocks, mineral compositions acquired during peak metamorphic stage (M2) are most likely found in the cores of garnet, cores of clinopyroxene, cores of plagioclase and cores of orthopyroxene. Compositions of rim parts of garnet grains and adjacent minerals, like

plagioclase, clinopyroxene, orthopyroxene and amphibole, are most likely related with retrograde stage (M3) metamorphism. As to the prograde metamorphic stage (M1), representative mineral compositions might not be able to survive the peak and retrograde metamorphic alteration. Therefore, in the following discussion, inferred mineral assemblages of M2 are garnet (core) + clinopyroxene (core) + plagioclase (core) + quartz while those of M3 are garnet (rim) + adjacent orthopyroxene + adjacent plagioclase.

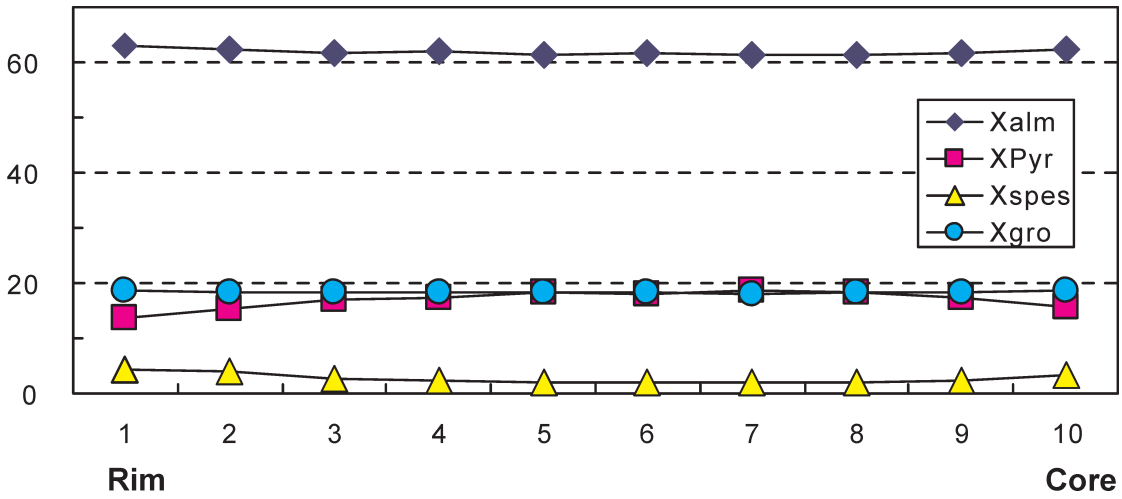

Fig. 7. Chemical zonation of garnet in sample EO182. alm-almandite, pyr-pyrope, spes-spessartite, gro-grossular.

Using compositions of minerals from two polished thin sections of sample EO182 (EO182a and EO182b) and in combination with geothermometers and geobarometers, metamorphic P and T conditions of each metamorphic stage are calculated. Related geothermometers and geobarometers are garnet – clinopyroxene – plagioclase – quartz geobarometers (Eckert et al., 1991; Newton and Perkins, 1982), garnet – orthopyroxene – plagioclase – quartz geobarometer (Bhattacharya et al., 1991), garnet – clinopyroxene geothermometers (Ellis and Green, 1979; Krogh, 1988; Powell, 1985; Ravna, 2000) and garnet – orthopyroxene geothermometer (Harley, 1984). The results are presented in Fig. 8. The paragenesis garnet-clinopyroxene-plagioclase-quartz

438 of sample EO182a yielded pressure conditions between 16 and 18 kbar and
439 temperatures from 930 to 960 °C (Fig. 8a), which lies in the field of high-pressure
440 granulite facies (O'Brien and Rötzler, 2003) or in the eclogite-high-pressure granulite
441 facies (E-HPG) field of Brown (2014). The retrogression paragenesis of EO182a
442 yielded pressures from 6.2 to 7.0 kbar and temperatures of 660 to 750 °C (Fig. 8b),
443 typical of the transition granulite to amphibolite facies. Sample EO182b gave
444 intermediate results with the higher and lower pressure ranges of 8-10 and 6.3-6.5 kbar,
445 respectively, and temperatures varying from 790 to 700 °C (Fig. 8c, d), also in the lower
446 pressure limit of the high-pressure granulite field (Fig. 9) to transition of normal
447 granulite to amphibolite facies. Pressure-temperature results of these two thin sections
448 plot on a clockwise retrograde P-T path (Fig. 9), consistent with the reaction textures of
449 the granulites.
450

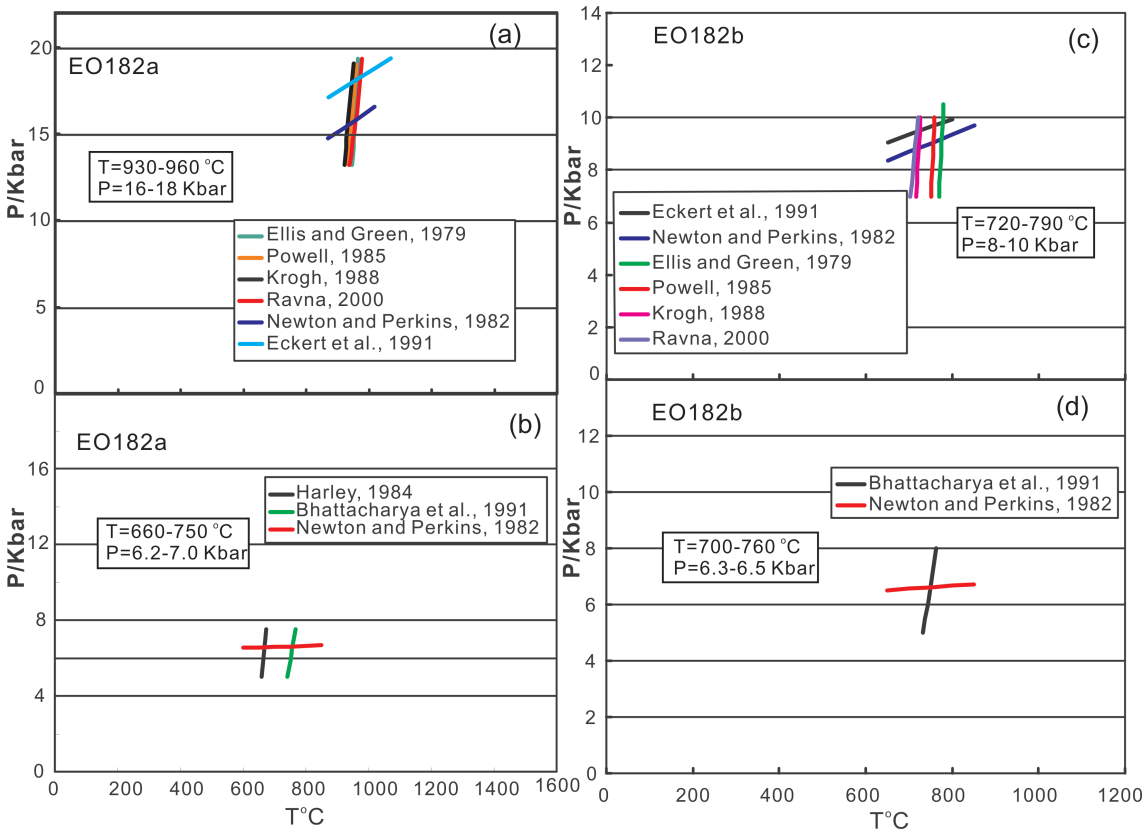

451

Fig. 8. Calculated P-T conditions of the mafic granulite EO182. (a) and (b) correspond to the high-, and low-pressure PT conditions of mineral reaction texture of thin section EO182a, respectively; (c) and (d) same for thin section EO182b.

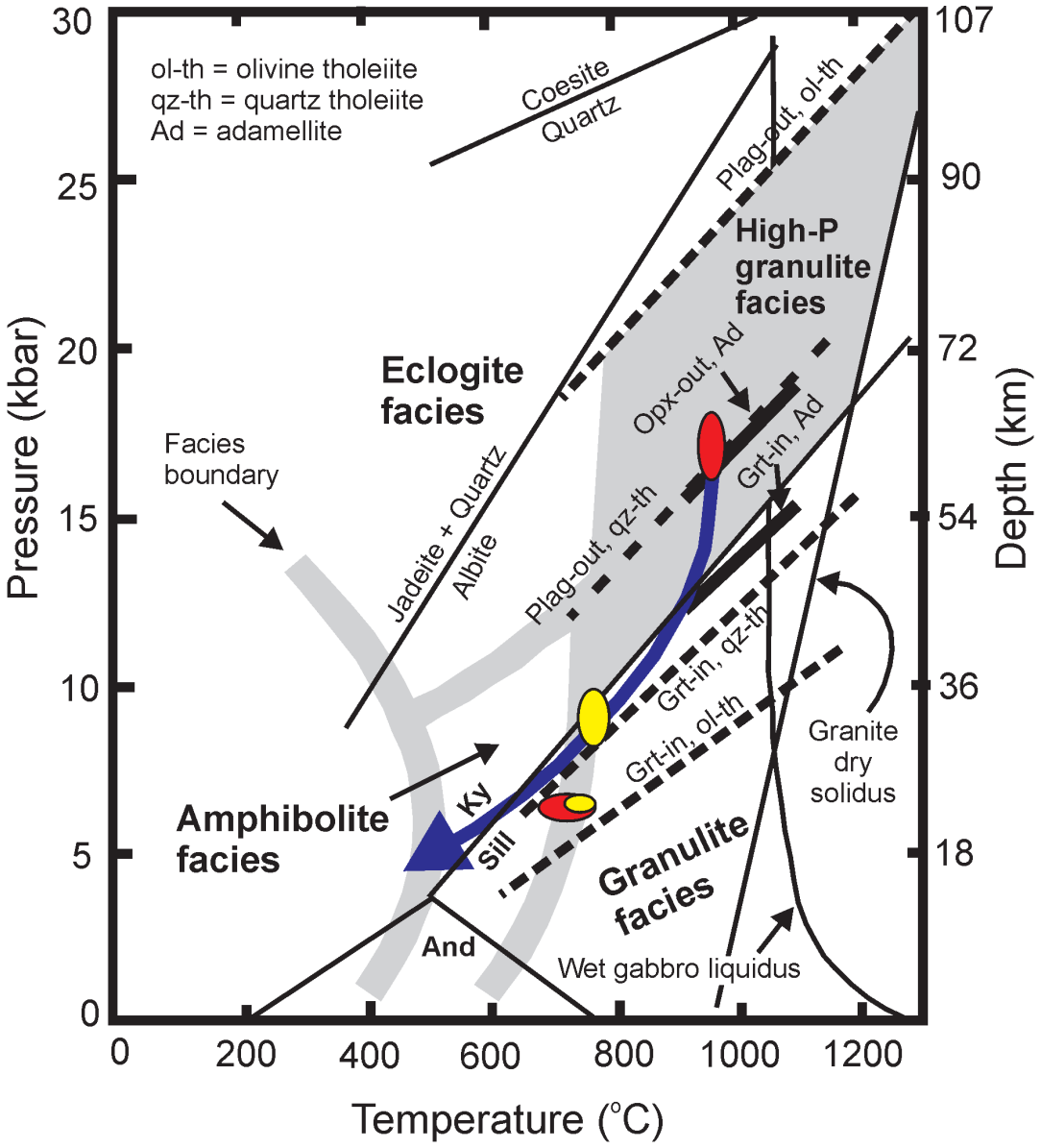

Fig. 9. P-T path of the mafic granulite samples plotted in the metamorphic facies diagram of O'Brien and Rötzler (2003). Red and yellow ellipses are PT conditions for samples EO182a and EO182b, respectively (see text for details). The blue thick arrow indicates a possible clockwise retrograde path for the mineral reaction textures.

4.2. Metamorphic conditions: Pressure-temperature pseudosections

Pressure-temperature pseudosections were calculated for sample EO182 bulk rock (Fig. 10). The phase field of Pl + Grt + Cpx + Ilm (red outline in Fig. 10) best represents the observed peak mineral assemblage. These pressure results overlap with 16-18 kbar obtained by thermobarometry for EO182a and with 8-10 kbar for EO182b (Fig. 8a). However, as there is a large uncertainty in the conventional thermobarometry for the same rock sample, the highest-pressure estimate may possibly be somewhat lower due to the absence of rutile in thin section. Thermobarometry for the lower-grade assemblage plot within the Opx stability field and indicate retrograde decompression and cooling.

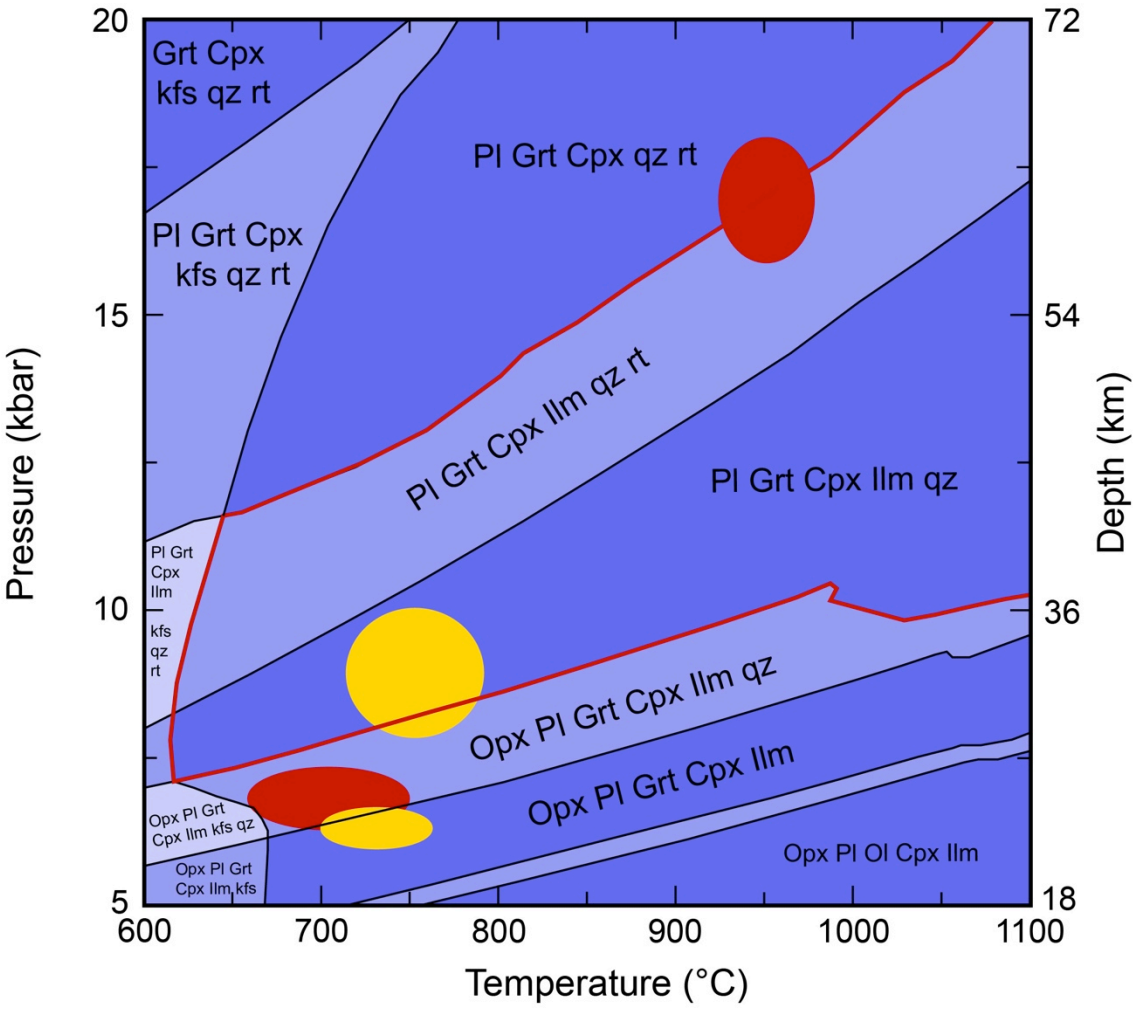

Fig. 10. Pseudosection for the bulk rock composition of sample EO182. Red outline marks the field with the observed granulite facies assemblage. Colours of the phase

476 fields represent the degree of variance ranging from four phases (darker blue) to seven
477 phases (pale blue). Red (EO182a) and yellow (EO182b) ellipses represent estimates
478 obtained from thermobarometry for high and low P-T conditions. Mineral
479 abbreviations: Cpx - clinopyroxene; Grt - garnet; Ilm - ilmenite; Ol - olivine; Opx -
480 orthopyroxene; Pl - plagioclase; kfs - K-feldspar; qz - Quartz; rt - rutile (capitalized:
481 solid solutions; lowercase: pure phases). Bulk composition of sample EO182 in wt.% is:
482 SiO2=44.92, TiO2=2.604, Al2O3=14.49, Fe2O3t=20.30, MnO=0.308, MgO=5.25,
483 CaO=10.04, Na2O=1.69, K2O=0.14, P2O5=0.478, LOI=-0.38, Total=100.22. Starting
484 composition in wt% (normalized to 100) for the system TiKNCFMASO is: SiO2=46.0,
485 TiO2=2.7, Al2O3=14.8, FeOt=18.7, MgO=5.4, CaO=10.3, Na2O=1.7, K2O=0.1,
486 O2=0.2.
487
488 **4.3. Zircon SHRIMP and LA-ICP-MS U-Pb geochronology, trace elements**
489 **geochemistry and Hf isotopes**
490 Five samples were collected for SHRIMP and LA-ICP-MS U-Pb zircon age
491 dating, of which one is high-pressure (HP) mafic granulite (EO182), three are
492 associated gneisses (14EW-20, 15GE-61, and EO178-D), and one trondhjemite sheet
493 (17ED-91) intrusive in the HP mafic granulite. Zircon inclusions in garnet from a
494 polished slab of sample EO182 were drilled to make another sample (EO182p) for
495 SHRIMP age dating. The results are shown in Table S3 (supplemental files). Zircon
496 grains from the HP mafic granulite EO182p were also analysed for rare earth elements
497 (REE) and other trace elements (Table S4 - Supplemental files). Concordant zircon
498 grains from HP mafic granulite EO182 and leucodioritic gneiss EO178-D were also
499 analysed for Hf isotopes; the results are shown in Table S5 (Supplemental files).
500 Cathodoluminescence images and spot ages of representative zircon grains of
501 the dated samples are shown in Fig. 11.

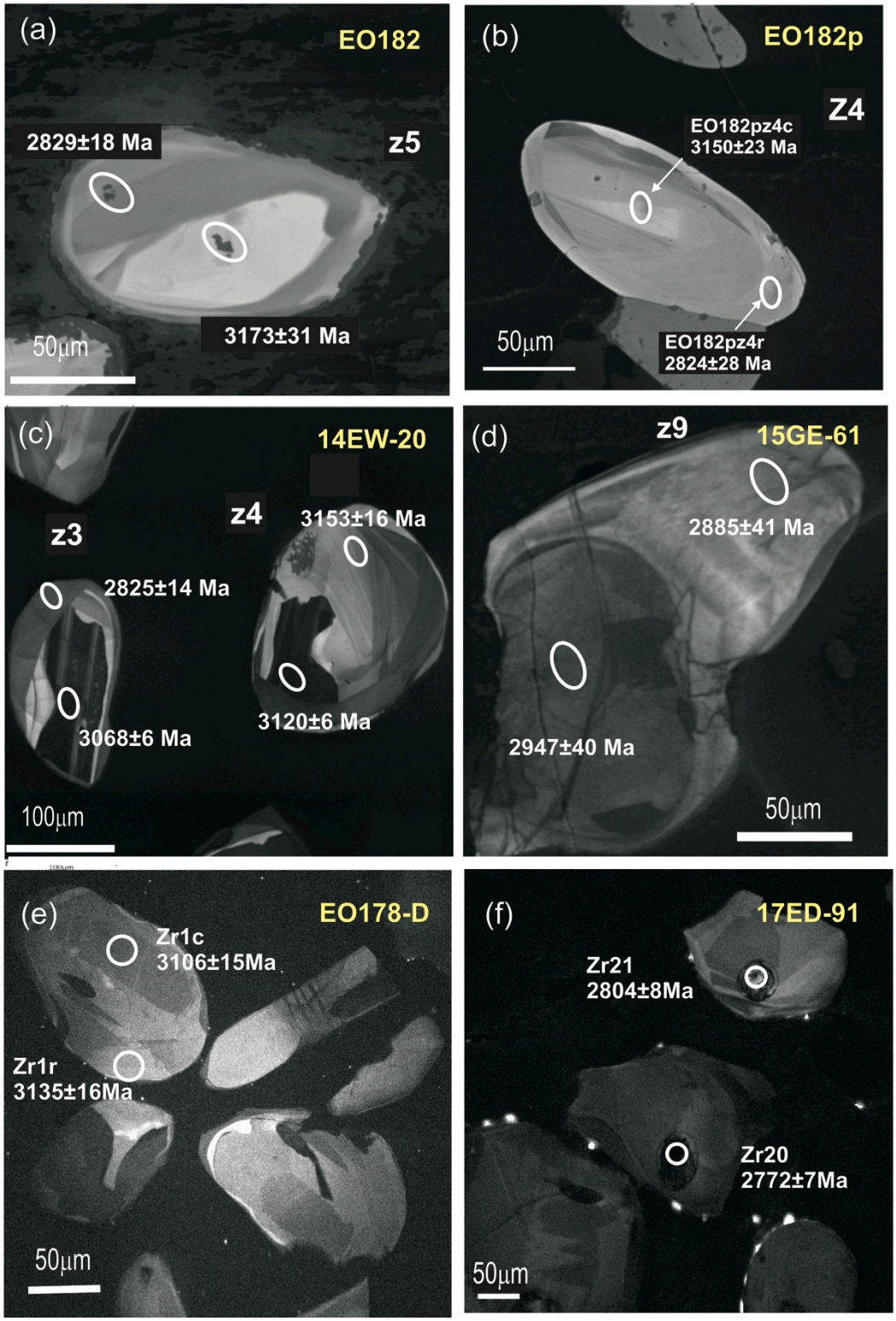

Fig. 11. Cathodoluminescence images and spot ages of selected zircon grains.

4.3.1. *Sample EO182 - High-pressure mafic granulite - SHRIMP*

This sample is a massive, garnet-rich mafic granulite. The youngest seventeen analyses (Table S3) of zircon grains target visible rim zones. These analyses yielded a

508 population at 2819 ± 14 Ma (MSWD = 1.2, probability = 0.22), which is considered the
509 best estimate of the age of the rims (Fig. 12a) grown during high-grade metamorphism
510 as discussed in the following section. The oldest and less abundant population in Fig.
511 12a comprises fifteen analyses of zircon core (e.g. Fig. 11a) with a mean $^{207}Pb/^{206}Pb$ age
512 of 3127 ± 14 Ma (MSWD = 1.4, probability = 0.16) that represents the best estimate of
513 the crystallization age of the protolith. A histogram with all ages is shown in Fig. 12b
514 where age peaks of core and rim analyses are highlighted. The intermediate concordant
515 ages are interpreted as Pb loss caused by incomplete solid-state recrystallization (e.g.
516 Vavra et al., 1996; Hoskin & Black, 2000; Möller et al., 2002) during the 2819 Ma
517 event.
518
519
520
521

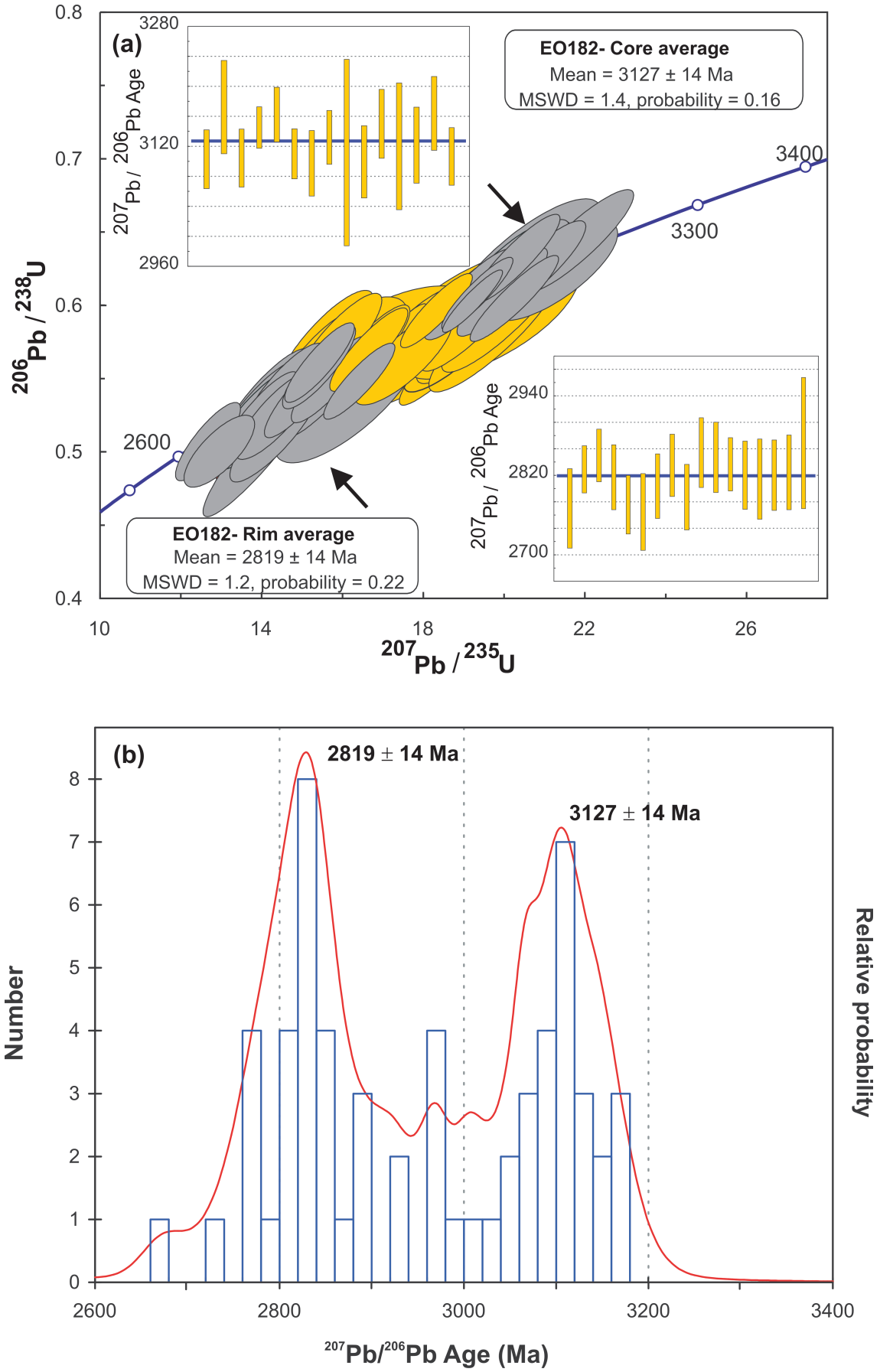

522

523 **Fig. 12.** SHRIMP U-Pb zircon ages for mafic granulite EO182. a) Concordia plot

524 showing age averages for core and rim zircons (grey ellipses); b) SHRIMP $^{207}Pb/^{206}Pb$

age histogram for metamorphic rims (2819 Ma) and older cores (3127 Ma) of zircon grains from sample EO182 and EO182p. The intermediate concordant ages are interpreted as Pb loss caused by incomplete solid-state recrystallization (e.g. Vavra et al., 1996; Hoskin & Black, 2000; Möller et al., 2002) during the 2819 Ma event.

4.3.2. *Sample EO182p -High pressure mafic granulite - SHRIMP*

SHRIMP analyses were performed on a polished slab of sample EO182, here named sample EO182p. A few zircon grains occur as inclusions in garnet. These grains and their host garnets were drilled and mounted in epoxy resin for SHRIMP age dating (Table S3; supplemental files) and LA-ICP-MS trace element analysis. As shown in Fig. 13a, the ages of the zircon core and rim spots were 3150 ± 23 Ma and 2824 ± 28 Ma, respectively. Although less precise due to limited data, within error limits, these ages replicate the average ages found above for sample EO182, i.e. 3127 ± 14 Ma on zircon cores, and 2819 ± 14 Ma on zircon rims.

Representative trace element data for some zircon grains included in garnet are shown in Table S4 (supplemental files). The location of the SHRIMP and LA-ICP-MS spots analysis are indicated in Fig.13a and Fig.13b, respectively, and the chondrite-normalized rare earth element (REE) patterns are shown in Fig. 13c. The REE patterns of rim and core spots differ significantly. The rim REE patterns show a lower heavy-REE abundance than those of the cores, a typical signature of zircon growth in equilibrium with another heavy-REE-rich mineral (e.g. Rubatto, 2002), which in this case is garnet. Therefore, we consider that the ca. 3130 Ma growth of zircon was in the absence of garnet, whereas the ca. 2820 Ma is the time of zircon growth in the presence of garnet, and by inference this is the age of the high-pressure metamorphic event.

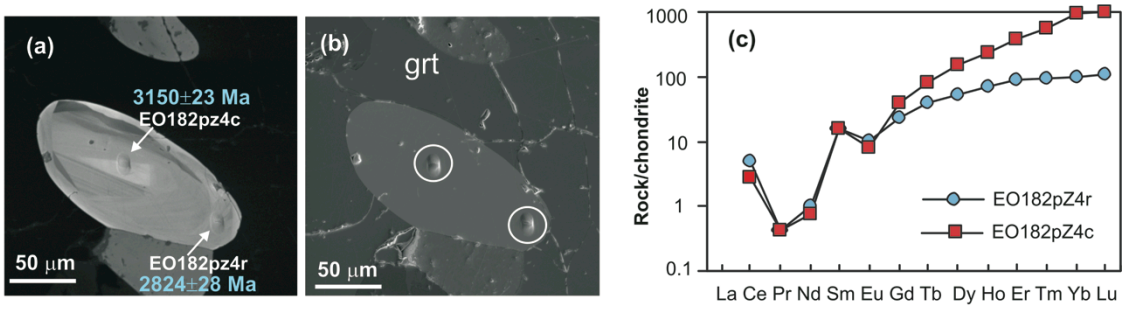

Fig. 13. Representative zircon grains as inclusions in garnet in sample EO182p. a) Cathodoluminescence image of a zircon core and rim with identification of the SHRIMP spots and $^{207}Pb/^{206}Pb$ ages; b) SEM backscatter image of the same zircon grain in (a) showing the SHRIMP (shallow pits) and the LA-ICP-MS analysed spots (white circles); c) Chondrite-normalised (McDonough and Sun, 1995) rare earth element patterns for the zircon grain in (b) showing the higher heavy rare earth element (HREE) abundances in the core spot (EO182pZ4c) than in the rim spot (EO182pZ4r).

On the basis of trace element data on zircon grains from oceanic gabbros and continental rocks, Grimes et al. (2007) suggested that the U vs. Yb, U/Yb vs Hf or Y plots can distinguish zircon crystallized in magmas emplaced in either tectonic settings. As shown in Fig. 14, the U vs. Yb and U/Yb vs Hf plots indicate that zircons of the HP mafic granulites may have crystallized from a magma emplaced in continental settings.

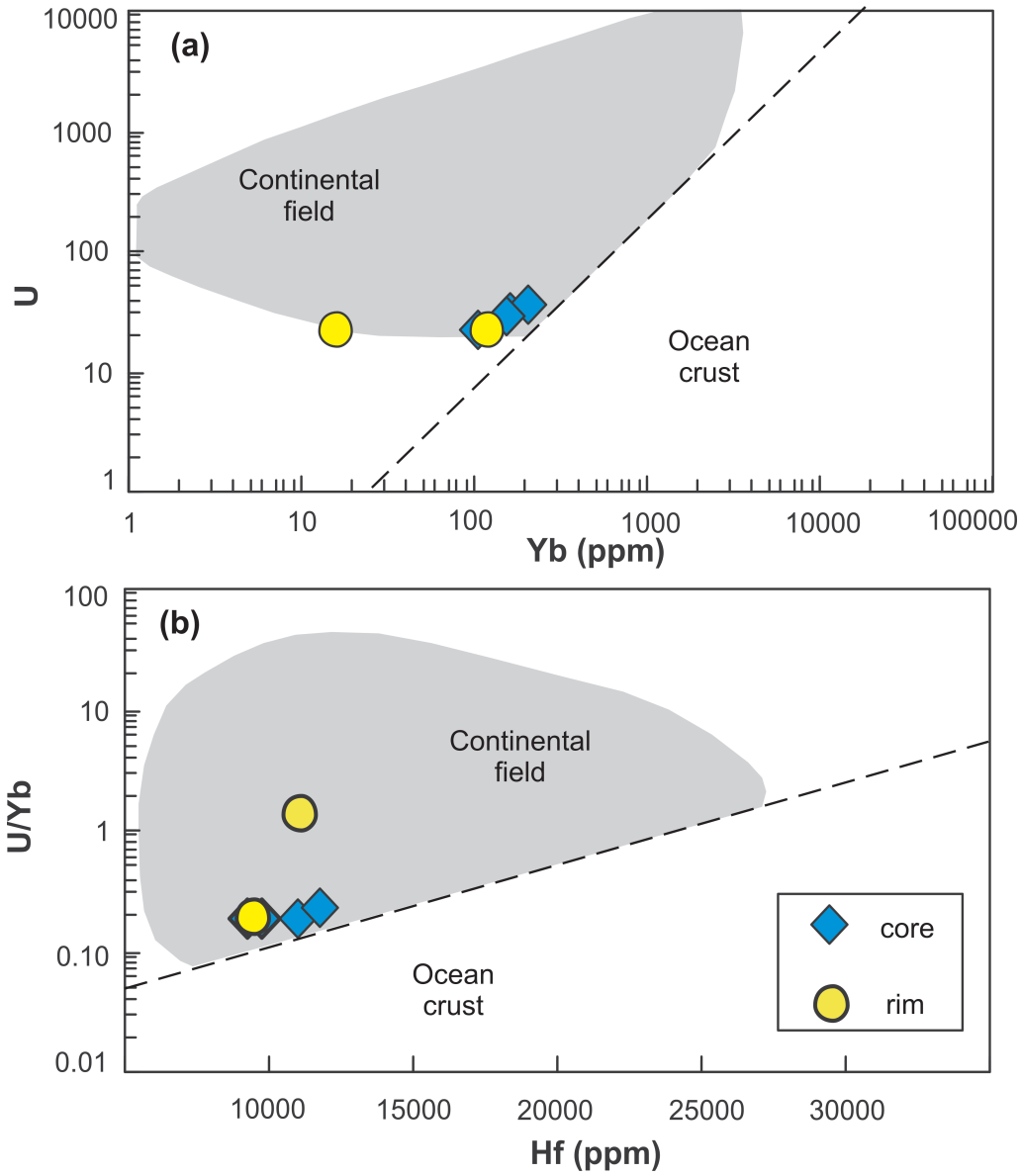

564

565 **Fig. 14.** Trace elements in zircon with fields of gabbros from oceanic crust and
566 continental rocks after Grimes et al. (2007). Data for zircon from the HP mafic
567 granulites plot all in the continental field.

568

569 **4.3.3.** ***Sample 14EW-20 - Host quartz-leucodiorite gneiss - SHRIMP***

570 Ten zircons were analysed and sixteen of twenty analyses yielded concordant
571 dates, which are spread from 2.83 to 3.13 Ga (Fig. 15a, Table S3). Five analyses plot in
572 a single population with a mean $^{207}Pb/^{206}Pb$ age of 3125 ± 15 Ma (MSWD=1.5,
573 probability = 0.20) (Fig. 15a). These analyses are from cores of complex zircons and
574 this age may represent the crystallization age of the protolith. There are also two

575 younger dates at 2.82 and 2.83 Ga from rims (Fig. 15a), which agree with the ~ 2.82 Ga
576 age of the metamorphism of the area as determined from samples EO182 and EO182p.
577 Furthermore, there are nine intermediate concordant dates ranging from 2.92 to 3.10 Ga
578 (Fig. 15a), which are interpreted as Pb loss caused by incomplete solid-state
579 recrystallization (e.g. Vavra et al., 1996; Hoskin & Black, 2000; Möller et al., 2002)
580 during the 2819 Ma event.
581
582 **4.3.4.** ***Sample 15GE-61 - Host leucodiorite gneiss - SHRIMP***
583 Twenty analyses, performed on fifteen zircons, yielded concordant dates ranging
584 from 2.83 to 3.26 Ga (Fig 15b; Table S3). There are five dates with ages from 2.83-2.88
585 Ga (Table S3; e.g. 15GE61z12), which broadly agree with the age of the metamorphism
586 of the area (i.e. ~2.82 Ga from sample EO182). There are also three dates at 3.11-3.12
587 Ga (Table S3; e.g. 15GE61z5c), which may be considered the crystallization age of the
588 protolith, and which match the other samples. Moreover, there are three older dates at
589 3.19-3.26 Ga, which may represent xenocrysts, but have not been observed in the other
590 samples. Apart from this, there are eight intermediate concordant dates between 2.94
591 and 3.06 Ga, which are interpreted as Pb loss caused by incomplete solid-state
592 recrystallization (e.g. Vavra et al., 1996; Hoskin & Black, 2000; Möller et al., 2002)
593 during the 2819 Ma event.
594
595
596 **4.3.5.** ***Sample EO178-D - Host leucodiorite gneiss - LA-ICP-MS***
597 Twenty-five zircon grains were analysed and twenty-two of thirty-two analyses
598 give concordant ages (±5% discordant; Table S3). Zircon CL images show sector field
599 zoning or unzoning (Fig. 11e); some grains show dark cores and bright rims. Thirteen,
600 less than 2% discordant zircon core analyses yielded an upper intercept date of 3104 ±

601 24 Ma (MSWD = 2.4; probability = 0.01) and four grains yielded a concordia age of
602 3138±20 Ma (Fig. 15c). Some grains yielded ca. 2.99 Ga rim dates and 3.06 Ga cores
603 (Table S3), which may be due to Pb loss. Only one zircon core analysis (z5, Table S3)
604 yielded a date of 2823 Ma comparable with the age of metamorphism observed in mafic
605 granulite EO182.

606 Combining the concordant data of the host gneisses (14EW-20, 15GE-61, and
607 EO178-D), two endmember age populations at 2.81-2.85 Ga and 3.08-3.15 Ga (Fig.
608 15d) can be distinguished. These populations can be also recognized in the HP mafic
609 granulite (Fig. 12). The youngest ages at 2.82-2.83 Ga is considered to represent the age
610 of metamorphism of this area. The oldest ages at 3.11-3.12 Ga, with an age cluster at
611 3120±6 Ma may be the crystallization age of the protolith. However, intermediate
612 concordant ages could be due to Pb loss caused by incomplete solid-state
613 recrystallization (e.g. Vavra et al., 1996; Hoskin & Black, 2000; Möller et al., 2002)
614 during the 2819 Ma event.
615
616
617

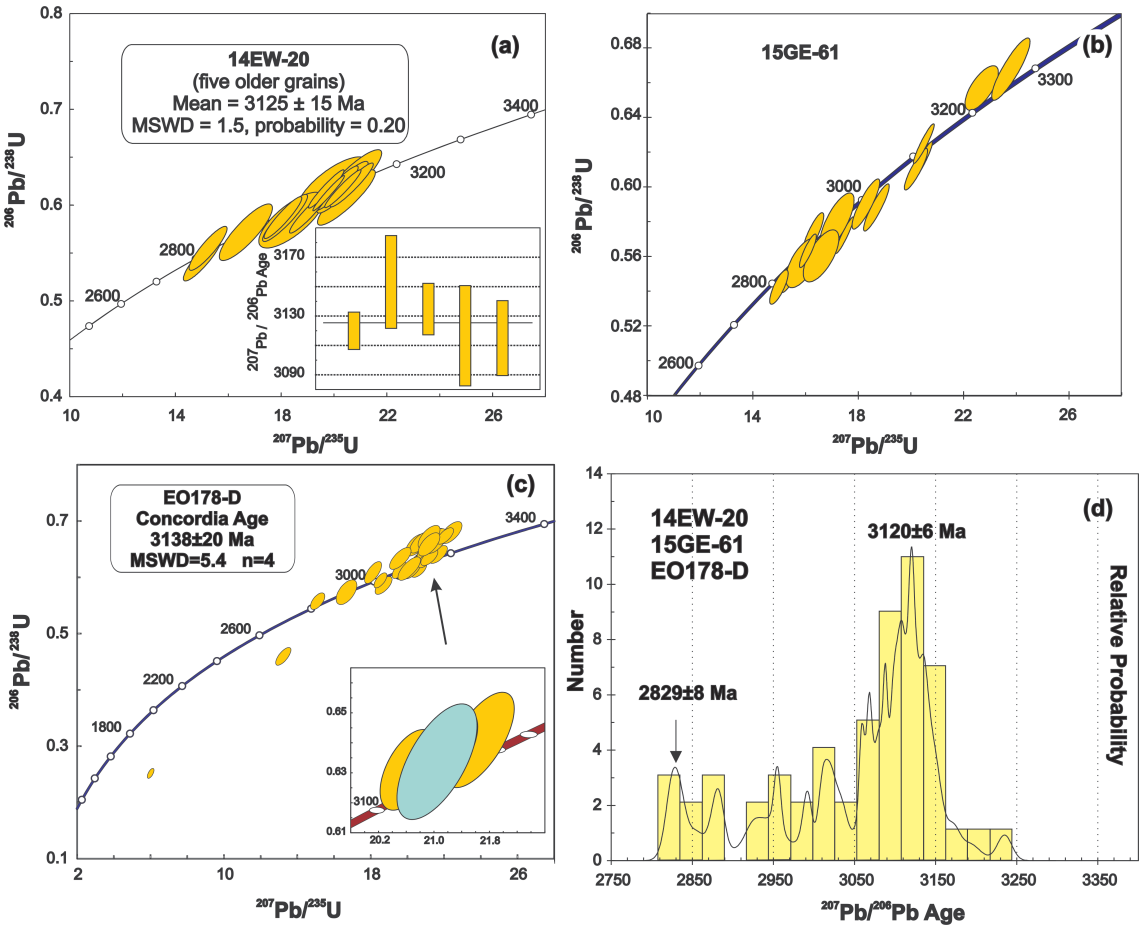

Fig. 15. SHRIMP and LA-ICP-MS U-Pb ages of diorite-leucodiorite gneisses associated with the HP mafic granulite. a) Concordia plot of zircon grains from sample 14EW-20 and a weighted average age of 3125 ± 15 Ma for the five oldest grains; b) Concordia plot for zircon grains from sample 15GE-61; c) Concordia plot for all zircon grains of sample EO178-D with concordia age shown in inset for the most concordant grains (<1% discordant); d) $^{207}Pb/^{206}Pb$ age histogram for the combined ages of samples 14EW-20, 15GE-61, and EO178-D.

4.3.6. *Sample 17ED-91 - Trondhjemite sheet intrusive in mafic granulite - LA-ICP-MS*

Twenty-one zircon grains were analysed and eleven had to be discarded due to high common Pb. From the remaining eleven zircon analyses (Table S3) only eight analyses give concordant ages (<5% discordant), of which one grain was considered

inherited (2927 Ma). The remaining seven analyses gave an upper intercept age of 2797 ± 5 Ma (MSWD = 1.12; probability = 0.34) and four grains less than 1% discordant gave a concordia age of 2793.6 ± 13 Ma (Fig. 16), which is considered the crystallization age of the trondhjemite sheets.

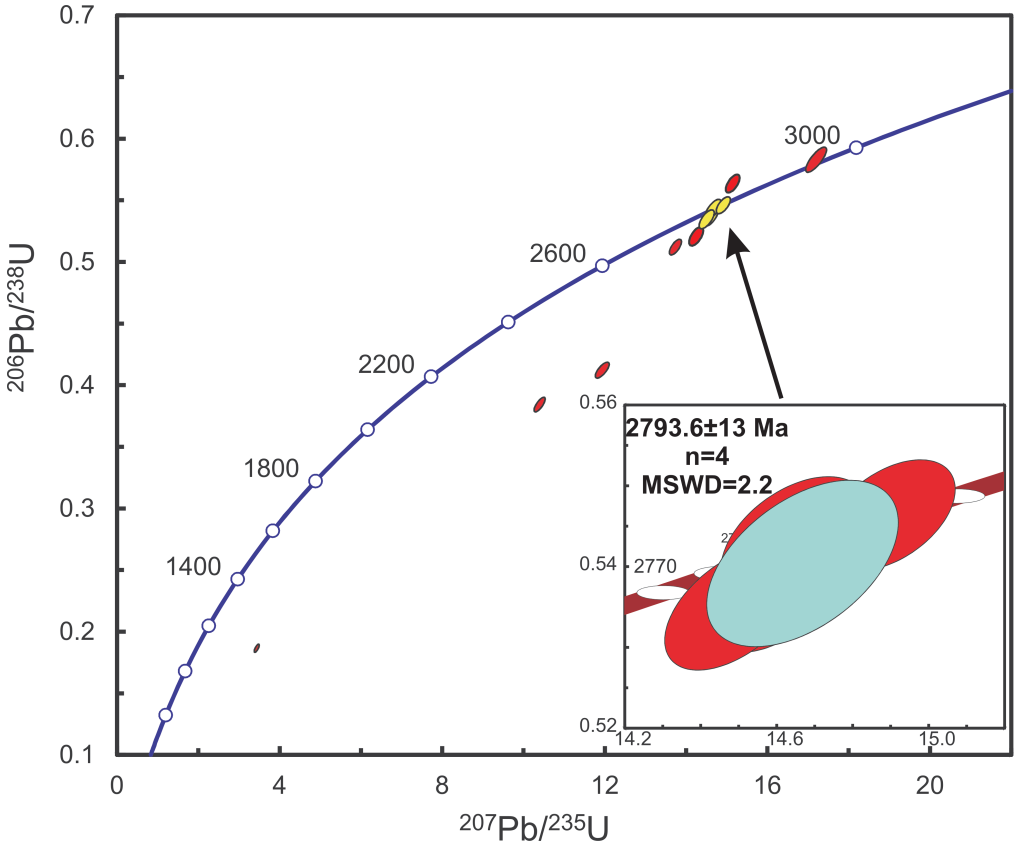

Fig. 16. LA-ICP-MS zircon U-Pb concordia age of 17ED-91 trondhjemite sheet intrusive in the HP mafic granulite.

4.3.7. *Hf isotopes results - LA-ICP-MS*

Zircon grains from two samples were analysed for Hf isotopes, namely the mafic granulite EO182 and leucodioritic gneiss EO178-D. The results are shown in Table S5. Depleted mantle (Blichert-Toft et al., 2010) and new crust (Dhuime et al., 2011) evolution are shown with the initial $\varepsilon_{Hf(t)}$ values of the mafic granulites and leucodioritic gneisses in Fig. 17. The Hf data come from the same location on

zircon grains that yielded concordant age data. The studied rocks show distinct $\varepsilon_{Hf(t)}$ values with mostly positive values (relative to CHUR) for the mafic granulite and negative values for the associated dioritic gneiss (Fig. 17). Field relationships (layering) indicate that the two rock types are co-magmatic, and yet they show different, although paralleling Lu-Hf isotopic evolution trends.

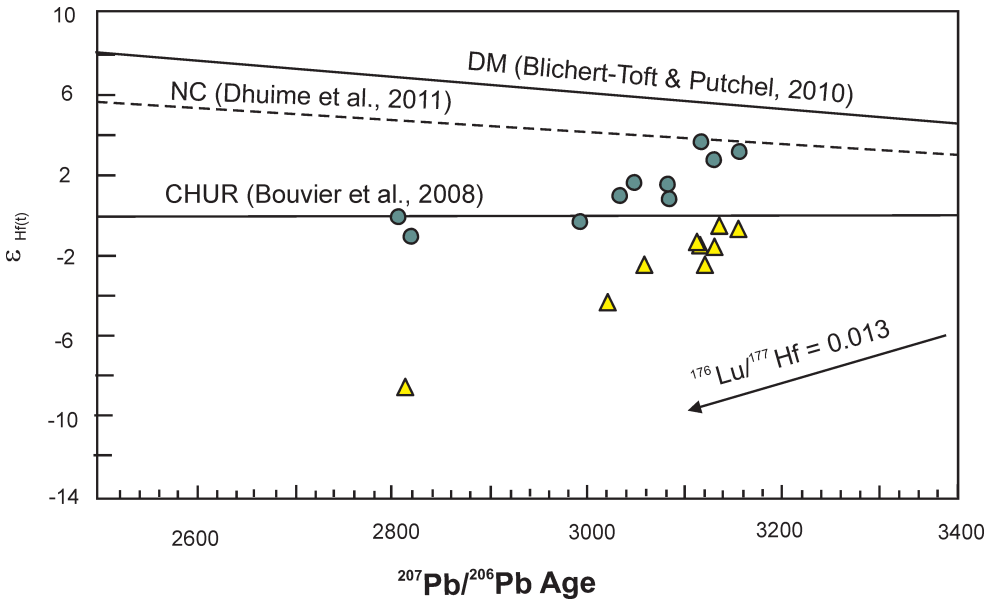

Fig. 17. Hf isotopes data for the Uauá HP mafic granulite EO182 (circle) and associated leucodioritic gneiss EO178-D (triangle). Two almost parallel trends are depicted for the studied samples, wherein the mafic granulite shows a clear juvenile component; the analyses close to 3120 Ma are representative of the protoliths age, those at 2.82 Ga are from metamorphic zircon rims, and intermediate ones are mixed ages due to Pb loss caused by incomplete solid-state recrystallization (e.g. Vavra et al., 1996; Hoskin & Black, 2000; Möller et al., 2002) during the 2.82 Ga event. All spot analyses were on locations that gave concordant analyses. Archaean upper crust growth $^{176}Lu/^{177}Hf$ value (0.013) after Condie et al. (2005).

5. Discussion

666 **5.1. Metamorphic conditions and global Archaean high-pressure granulites**

667 The Uauá mafic granulite occurs as sheet-like bodies (locally with discrete
668 igneous layering), or lenses in structural conformity with ca. 3120 Ma-old leucodiorite
669 to quartz-diorite gneisses and ca. 2800 Ma trondhjemite sheets. The mafic granulite has
670 a relic high-pressure (HP) granulite facies assemblage of garnet-clinopyroxene with
671 minor quartz, plagioclase and ilmenite. This paragenesis reached the HP metamorphic
672 equilibrium about 16-18 kbar and 950°C ca. 2820 Ma ago, according to our
673 thermobarometry and pseudosections calculations and the SHRIMP U-Pb age dating of
674 zircon rims that have grown in equilibrium with garnet. Garnet porphyroblasts have a
675 corona of orthopyroxene-plagioclase symplectites, a textural relationship, which, when
676 combined with minor hornblende in the symplectites and along the granulite foliation,
677 defines retrogression from HP granulite facies through normal granulite facies to
678 transition to amphibolite facies conditions of 6.2 to 7.0 kbar and 660 to 750 ^{o}C.

679 High-pressure metamorphic rocks in the Archaean are not common. The oldest
680 high-pressure metamorphic rock in upper crustal greenstone belts is a 3200 Ma meta-
681 volcanic amphibolite from the Barberton belt in South Africa with a HP condition of
682 12-15 kbar at a relatively low temperature of 600-650°C (Moyen et al., 2006). Another
683 example can be found in the Belomorian province of Russia where high-pressure
684 granulite (retrogressed eclogite) lenses in gneisses have been described as Archaean but
685 the metamorphic age is contentious. Accordingly, Volodichev et al. (2004), Mints et al.
686 (2010, 2014), Dokukina et al. (2012), and Li et al. (2015) suggested from zircon dating
687 that the HP metamorphism was Archaean (between 2870 and 2710 Ma). However, on
688 the basis of Lu-Hf isochron dating of eclogite garnet (Herwartz et al., 2012, Yu et al.,
689 2019), garnet-whole rock Sm-Nd isochron and zircon U-Pb of garnetites (Mel'nik et al.,
690 2013), U-Pb zircon dating with omphacite + garnet inclusions (Imayama et al., 2017),
691 and metamorphic zircon rims surrounding Archaean magmatic zircon cores (Skublov et

al. 2010, 2011) these authors provided evidence for the high-grade metamorphism at ca. 1900-1920 Ma.

Many other high-pressure granulites have yielded ages that straddle the Neoarchaean-Palaeoproterozoic transition, such as meta-pelitic granulites in the Limpopo belt (ca. 2700 Ma; Van Reenen et al., 1987; Droop, 1989), mafic granulites in the Athabasca terrane, Canada (ca. 2550 Ma; Baldwin et al., 2006; Williams et al., 2009), the North China Craton (2520 Ma at Yinshan, Wang and Guo, 2017; 2510 Ma at Hebei, Kwan et al., 2016; 2500 Ma at Jianping, Wei et al., 2001; 2473 Ma at Jiaodong, Liu et al., 2015), the Lewisian in Scotland (ca. 2480 Ma, Sajeev et al., 2013), and in India (2780 Ma in the Bundelkhand craton, Saha et al., 2011; 2541 Ma at Sittampundi, Sajeev et al., 2009; ca. 2490 Ma in the Salem block, Anderson et al., 2012; ca. 2460 Ma in the Nilgiri Block, Samuel et al., 2015). As such, the Uauá HP mafic granulite, with the age of ca. 2820 Ma is the World's second oldest HP mafic granulite, and possibly records significantly higher pressures and temperatures than the oldest.

5.2. Crustal thickening and geodynamic scenario

Thermodynamic derived pressure estimates for equilibrium of metamorphic assemblages can be linked to the lithostatic pressure, which in turn can be directly related to depth (e.g. Jolivet et al., 2003). This general assumption of metamorphic petrology has been challenged recently due to the suggestion that tectonic deformation (differential stress, non-hydrostatic stress) can produce larger pressures than lithostatic pressure (e.g.; Schamalholz and Podladchikov, 2014; Wheeler, 2014; Tajcmanová, 2015; Reuber et al., 2016). However, for lower crustal rocks where permeability and porosity may be exceedingly small (Ingebritsen and Manning, 2002), the mean stress is not far from the vertical stress in value, and the pressure versus depth interpretation applies (Wheeler, 2014). Moreover, on a recent account about equilibrium in non-

718 hydrostatic metamorphic systems, Powell et al. (2018) concluded that calculations that
719 incorporate the equilibrium thermodynamics of non-hydrostatically stressed minerals
720 yield results very similar to those assuming hydrostatic stress, and as such the estimated
721 pressure may be related to the depth of metamorphism.

722 In this study, the pressure estimates using the thermobarometers of Eckert et al.
723 (1991) and Newton and Perkins (1982) indicate pressures of 16-18 kbar for the high-
724 pressure mineralogy (Fig. 8-9), which was corroborated by quantitative phase diagrams
725 (pseudosections - Fig. 10). This pressure range suggests a crustal thickness of about 60
726 km (Fig. 9, 10), which in the Phanerozoic is found in accretionary and collisional
727 orogens. The clockwise retrogression path of the studied granulites from high-pressure
728 granulite facies through normal granulite facies to amphibolite facies (Fig. 9) is also
729 consistent with crustal thickening in collisional orogens followed by tectonic
730 exhumation (e.g. Carswell and O'Brien, 1993; Barker, 1998; Liu et al., 2013).

731 How thick was the crust in the Archaean and how it became thick to form the
732 first cratons and supercratons; whether by subduction, collision, underplating, or
733 intracontinental thrusting, it is a subject of current debate (e.g. Smirnov et al., 2013;
734 Brown 2014; Sizova et al., 2015; Tang et al., 2016; Johnson et al., 2017). However,
735 there is growing evidence that plate tectonics became global between 3.0 Ga and 2.5
736 Ga, and could produce a thick lithosphere required to form Archaean high-pressure
737 granulites and eclogites (e.g. Van Kranendonk et al., 2007; Burke, 2011; Polat, 2013).
738 For example, Shirey and Richardson (2011) reported the first occurrence of ca. 3.0 Ga
739 eclogitic garnet with basaltic Re/Os ratios (2-30 as opposed to peridotitic ratios of 0.01-
740 0.03) as inclusions in diamonds; Dhuime et al. (2012) recognized the increase of
741 recycling of crust into the mantle by 3.0 Ga probably through subduction at convergent
742 plate margins; Moyen et al. (2006) suggested that the high-pressure and relatively low
743 temperature of 3200 Ma amphibolite from the Barberton belt, in Africa, supported the

744 operation of subduction-driven processes in the Archaean; and Brown (2006) suggested
745 that the first appearance of ultrahigh-temperature (UHT) and medium-temperature
746 eclogite–high-pressure (EHP) granulite metamorphism in the Neoarchaean marks the
747 onset of plate tectonics ("Proterozoic plate tectonics" to distinguish from modern plate
748 tectonics that is marked by ultrahigh-temperature and ultrahigh-pressure
749 metamorphism). Evidence for the punctuated operation of plate tectonics in the Early
750 Archaean has been well reported (e.g. Komiya et al., 1999, 2015; Polat et al., 2009;
751 O'Neill et al., 2013), and it is currently increasingly accepted that some kind of global
752 plate tectonics, either of Proterozoic-type regime (Brown, 2006; 2009; 2014; Brown and
753 Johnson, 2018) or modern-type regime was in wide operation between 3.0-2.5 Ga. The
754 shallow dipping, 2820 Ma-old Uauá high-pressure mafic granulites and their ca. 3120
755 Ga protoliths formed approximately during this period, and they may shed some lights
756 into models of crustal evolution in the Archaean.

757 The following petrogenetic constraints suggest that the igneous protoliths of the
758 Uauá HP mafic granulites and associated leucodiorite gneiss were emplaced in a
759 continental tectonic setting. Firstly, the Uauá high-pressure mafic granulite crops out as
760 sheets interleaved with leucodiorite- and quartz-diorite gneisses. These rocks grade into
761 each other through a layered zone (Fig. 5a), which indicates they belong to a plutonic
762 igneous complex. The igneous protoliths of these rocks have a similar age (3127±14 Ma
763 for the mafic granulite and 3120±6 Ma for the leucodiorite gneiss) but the leucodiorite
764 gneiss contain older inherited zircon grains (3.19-3.26 Ga). Secondly, U, Yb, and Hf
765 contents in zircon grains from the mafic granulite (Fig. 13) indicate that zircon grew in
766 continental settings rather than in the ocean crust. Thirdly, Hf isotopes in zircon yield
767 positive $\varepsilon_{Hf(t)}$ values for the mafic granulite and negative values for the associated
768 leucodiorite gneiss; zircon positive $\varepsilon_{Hf(t)}$ values indicate magmas derived direct from the
769 mantle, whereas negative values imply more complex processes, such as crustal

770 contamination of mantle magmas and reworking of older crust (e.g. Dhuime et al.,
771 2012; Iizuka et al., 2017).

772 Given that field relationships (layering) show that the protoliths of the two rock
773 types belong to a single igneous complex, then there are three possibilities to explain the
774 observed contrasting zircon Hf isotope signatures. The first possibility is that the
775 emplacement of the parental, mantle-derived basic magma of the mafic granulite into an
776 older continental crust was accompanied by partial melting of this older crust to produce
777 the dioritic magma that was subsequently mixed with the resident basic magma. The
778 second possibility is that the emplacement of a single parental basic magma in older
779 continental crust was followed by fractional crystallization of this magma to produce
780 the more evolved leucodiorite, which in turn would interact/contaminate with older
781 rocks. The third possibility is that a juvenile basic magma emplaced into a leucodioritic
782 magma chamber that was contaminated with older continental crust. The latter
783 possibility is preferred for many reasons: i) the occurrence of continental crust older
784 than the protolith age (ca. 3.12 Ga) of the studied rocks in the Uauá area is very much
785 likely because three zircon grains with ages of ca. 3.2-3.3 Ga were found in the
786 leucodiorite gneiss 14EG-61 (Table S3); and ii) the igneous protoliths of the mafic
787 granulite and associated diorite gneiss were arguably derived from two magma types as
788 suggested by their distinct Hf isotope signatures in zircon (Fig. 17). Having concluded
789 that the protoliths of the mafic granulite and associated leucodiorite gneiss might have
790 emplaced in an older continental crust, another relevant issue to be discussed is the
791 relatively shallow-dipping foliation observed in the studied rocks.

792 Shallowly dipping foliation in granulite facies terrains has been described in
793 both contractional (e.g. Dumond et al., 2010; Masquelin et al., 2017) and extensional
794 (Harris et al., 2002; Arango et al., 2013) tectonic settings. Foliation of the Uauá HP
795 mafic granulite and associated leucodiorite gneiss dips 5-25^{o} to NE-SE with quartz or

796 feldspar stretching lineation plunging to NE (Fig. 3). Locally, more deformed
797 leucodiorite gneiss shows subhorizontal, decimetre-thick mylonite bands with top-to-
798 SW kinematics (Fig. 5d) suggesting that contraction was probably active during and
799 after the high-pressure granulite metamorphism. Exhumation of the HP rocks was
800 accompanied by extensive retrogression to normal granulite and amphibolite facies, and
801 might have taken no more than 20 million years as indicated by intrusion of
802 trondhjemite sheets in the retrogressed granulite/amphibolite facies rocks ca. 2800 Ma.
803 Consequently, and using the pressure-depth relationship shown in Fig. 9, the
804 exhumation rate from high-pressure granulite to amphibolite facies was about 2
805 mm/year, a number comparable to Phanerozoic exhumation velocities of subducted
806 oceanic crust (Agard et al., 2009). We suggest that the mafic and felsic igneous
807 protoliths of the mafic granulite and leucodiorite gneiss were deformed and
808 metamorphosed by contraction and crustal thickening during collision of blocks/terranes
809 not yet constrained. Later, the resulting larger continental block accreted to other blocks
810 or cratons to form one of Earth's first supercratons by the end of the Mesoarchaean.

811 Bleeker (2003) coined the name "supercratons" to include all large ancestral
812 landmasses of Archaean age with a stabilized core that on break-up spawned several
813 independently drifting cratons. The oldest supercraton was probably Vaalbara (Cheney,
814 1996) that cratonized about 3.0 Ga (Moser et al., 2001); its descendants are the
815 Kaapvaal, Pilbara, and possibly also the Singhbhum craton in India (Kumar et al.,
816 2017). The next supercratons in age are Sclavia and Superia, which cratonized about 2.6
817 Ga and 2.65 Ga (Bleeker, 2003), respectively. Brown (2006, 2007) observed that the
818 formation of the supercratons Superia and Sclavia, and of the supercontinents Nuna,
819 Rodina, and Gondwana was shortly preceded by periods of eclogite-high-pressure
820 granulite metamorphism. Therefore, the Uauá terrane, with its 2820 Ma high-pressure
821 mafic granulite occurrences, may represent a fragment of the root of a major Archaean

822 supercraton formed at the end of the Mesoarchaean, or most probably at the dawn of the
823 Neoarchaean. Salminen et al. (2018) have recently discussed this possibility. Using
824 magmatic age barcode comparisons, cratonization ages, paleomagnetism and age of
825 mafic dyke swarms, Salminen et al. (2018) propose that the northern São Francisco
826 (Uauá block), Kaapvaal and Pilbara cratons were nearest neighbours in the
827 Mesoarchaean, and along with other cratons (Superior, Karelia + Kola, Zimbabwe,
828 Yilgarn, Tanzania) they all were probably part of the Archaean supercraton
829 Supervaalbara of Gumsley (2017).
830
831 **6. Conclusions**
832 1) Uauá mafic granulite occurs as sheet-like bodies (locally with discrete igneous
833 layering), or lenses in structural conformity with leucodiorite to quartz-diorite
834 gneisses and crosscut by ca. 2800 Ma trondhjemite sheets.
835 2) Igneous protoliths of the mafic granulite and associated leucodiorite gneiss may
836 belong to a single igneous complex ca. 3120 Ma old, possibly emplaced in a
837 continental setting.
838 3) Mafic granulite has a relic high-pressure granulite facies assemblage of garnet-
839 clinopyroxene with minor quartz, plagioclase and ilmenite. This paragenesis reached
840 the metamorphic equilibrium about 16-18 kbar and 930-960°C ca. 2820 Ma ago.
841 4) Garnet porphyroblasts have a corona of orthopyroxene-plagioclase symplectites, a
842 textural relationship, which, when combined with minor amphibole in the
843 symplectites and hornblende blades oriented along the granulite foliation, defines
844 retrogression to 6.2 to 7.0 kbar and 660 to 750 ^{o}C in the granulite to amphibolite
845 facies transition.
846 5) Exhumation from high-pressure conditions to normal granulite and amphibolite
847 facies has probably taken no more 20 million years at a rate of about 2 mm/year, a

number comparable to Phanerozoic exhumation velocities of subducted oceanic crust.

6) Uauá high-pressure mafic granulite, with the age of ca. 2820 Ma is the World's second oldest HP mafic granulite.

7) Crustal thickening due to blocks/cratons collision to form the high-pressure granulite possibly was in operation in the late Mesoarchaean preceding the formation of Earth's first supercratons.

Acknowledgements

This research was funded by FAPESP thematic project "Evolution of Archaean Terranes of the São Francisco Craton and the Borborema Province, Brazil: global environmental and geodynamic implications" (grant # 2012/15824-6) and FAPESP-ATN project "4D evolution of mineralization in Archaean Terranes of Brazil" (grant # 2014/50353-0). The Brazilian National Research Council (CNPq) is acknowledged for research grants to EPO (# 305658/2015-8) and WSA (# 312509/2014-6). The Australian Research Council and a university-government consortium is acknowledged for support of the SHRIMP facilities. We thank Editor Wilson Teixeira and two anonymous journal reviewers for their scientific input and constructive reviews, which greatly helped to improve the manuscript. This paper is dedicated to the memory of Prof. John Tarney, from University of Leicester, who has inspired several geologists with his talent and creativity on the geology of Archaean terranes.

Appendix A. Supplementary data (tables S1-S5): Sample location (Table S1); Mineral composition (Table S2); Zircon U-Pb data (Table S3); Zircon trace element (Table S4); Zircon Hf isotope data (Table S5);

874 **References**

875

876 Agard P., Yamato P., Jolivet L., Burov E., 2009. Exhumation of oceanic blueschists and
877 eclogites in subduction zones: Timing and mechanisms. Earth-Science Reviews 92,
878 53–79.

879 Albert C., Farina F., Lana C., Stevens G., Storey C., Gerdes A., Dopico, C.M., 2016.
880 Archean crustal evolution in the Southern São Francisco craton, Brazil: Constraints
881 from U-Pb, Lu-Hf and O isotope analyses. Lithos 266–267, 64–86.

882 Anderson J.R., Payne J.L., Kelsey D.E., Hand M., Collins A.S., Santosh M., 2012.
883 High-pressure granulites at the dawn of the Proterozoic. Geology 40, 431-434.

884 Arango C., Fernández R.D., Ricardo Arenas R., 2013. Large-scale flat-lying isoclinal
885 folding in extending lithosphere: Santa María de la Alameda dome (Central Iberian
886 Massif, Spain) Lithosphere 5, 483-500.

887 Baldwin J.A., Bowring S.A., Williams M.L., Mahan K.H., 2006. Geochronological
888 constraints on the evolution of high-pressure granulites from an integrated electron
889 microprobe and ID-TIMS geochemical study. Lithos 88, 173-200.

890 Barker A.J., 1998. Introduction to Metamorphic Textures and Microstructures. Second
891 Edition. Routledge, Taylor & Francis Group.

892 Bhattacharya A., Krishnakumar K., Raith M., Sen S., 1991. An Improved Set of a-X
893 Parameters for Fe-Mg-Ca Garnets and Refinements of the Orthopyroxene-Garnet
894 Thermometer and the Orthopyroxene-Garnet-Plagioclase-Quartz Barometer.
895 Journal of Petrology 32, 629-656.

896 Black L.P., Kamo S.L., Allen C.M., Aleinikoff J.N., Davis D.W., Korsch R.J.,
897 Foudoulis, C., 2003. TEMORA 1: a new zircon standard for Phanerozoic U-Pb
898 geochronology. Chemical Geology 200, 155-170.

899 Bleeker W., 2003. The late Archean record: a puzzle in ca. 35 pieces. Lithos 71, 99–
900 134.
901 Blichert-Toft J., Puchtel I.S., 2010. Depleted mantle sources through time: Evidence
902 from Lu–Hf and Sm–Nd isotope systematics of Archean komatiites. Earth and
903 Planetary Science Letters 297, 598–606.
904 Bouvier A., Vervoort J.D., Patchett P.J., 2008. The Lu–Hf and Sm–Nd isotopic
905 composition of CHUR: Constraints from unequilibrated chondrites and
906 implications for the bulk composition of terrestrial planets. Earth and Planetary
907 Science Letters 273, 48–57.
908 Brown M., 2006. Duality of thermal regimes is the distinctive characteristic of plate
909 tectonics since the Neoarchean. Geology 34, 961–964.
910 Brown M., 2007. Metamorphism, plate tectonics, and the supercontinent cycle. Earth
911 Science Frontiers 14, 1–18.
912 Brown M., 2009. Metamorphic patterns in orogenic systems and the geological record.
913 In: Cawood, P.A. & Kröner, A. (eds) Earth Accretionary Systems in Space and
914 Time. The Geological Society, London, Special Publications,318, 37–74.
915 Brown M., 2014. The contribution of metamorphic petrology to understanding
916 lithosphere evolution and geodynamics. Geoscience Frontiers 5, 553-569.
917 Brown M., Johnson T., 2018. Secular change in metamorphism and the onset of global
918 plate tectonics. American Mineralogist 103, 181–196.
919 Burke K., 2011. Plate tectonics, the Wilson cycle, and Mantle plumes: geodynamics
920 from the top: Annual Review of Earth and Planetary Sciences 39, 1–29.
921 Carswell D. A., O'Brien P. J., 1993. Thermobarometry and Geotectonic Significance of
922 High-Pressure Granulites: Examples from the Moldanubian Zone of the Bohemian
923 Massif in Lower Austria. Journal of Petrology 34, 427–459.

924 Cheney E.S., 1996. Sequence stratigraphy and plate tectonic significance of the
925 Transvaal succession of Southern Africa and its equivalent in Western Australia.
926 Precambrian Research 79, 3–24.
927 Claoue-Long J.C, Compston W., Roberts J., Fanning C.M., 1995. Two Carboniferous
928 ages: A comparison of SHRIMP zircon dating with conventional zircon ages and
929 40Ar/39Ar analysis. Geochronology, Timescales and Global Stratigraphic
930 Correlation. W.A. Berggren, Kint, D.V., Aubry, M.P. Hardenbol, J., Society for
931 Sedimentary Geology Special Publications. 54, 3-21.
932 Compston W., Williams I.S., Meyer C.E., 1984. U-Pb geochronology of zircons from
933 lunar breccia 73217 using a sensitive high-mass resolution ion microprobe.
934 Proceedings of the fourteenth Lunar and Planetary Science Conference, Part 2.
935 Journal of Geophysical Research. (No more details?)
936 Condie K.C., 2011. Earth as an evolving planetary system. Academic Press, Elsevier,
937 574 p.
938 Condie K.C., Beyer E., Belousova E., Griffin W.L., O'Reilly S.Y., 2005. U–Pb isotopic
939 ages and Hf isotopic composition of single zircons: The search for juvenile
940 Precambrian continental crust. Precambrian Research 139, 42–100.
941 Connolly J.A.D., 2005. Computation of phase equilibria by linear programming: A tool
942 for geodynamic modeling and its application to subduction zone decarbonation.
943 Earth and Planetary Science Letters 236, 524–541.
944 De Laeter J.R., Kennedy A.K., 1998. A double focussing mass spectrometer for
945 geochronology. International Journal of Mass Spectrometry 178, 43-50.
946 De Paoli M.C., Clarke G.L., Klepeis K.A., Allibone A. H., Turnbull I.M., 2009. The
947 Eclogite-Granulite Transition: Mafic and Intermediate Assemblages at Breaksea
948 Sound, New Zealand. Journal of Petrology 50, 2307-2343.

949 Dhuime B., Hawkesworth C.J., Cawood P.A., 2011. When Continents Formed. Science
950 331, 154-155.
951 Dhuime B., Hawkesworth C.J., Cawood P.A., Storey C. D., 2012. A change in the
952 geodynamics of continental growth 3 billion years ago. Science 335, 1334–1336.
953 Dickinson W., Gehrels G., 2003. U-Pb ages of detrital zircons from Permian and
954 Jurassic eolian sandstones of the Colorado Plateau, USA: Paleogeographic
955 implications. Sedimentary Geology 163, 29–66.
956 Dilek Y., Furnes H., 2014. Evolution of Archean Crust and Life. Springer, Dordrecht.
957 Dokukina K.A., Bayanova T.B., Kaulina T.V., Travin A.V., Mints M.V., Konilov A.N.,
958 Serov P.A., 2012. The Belomorian eclogite province: sequence of events and age of
959 the igneous and metamorphic rocks of the Gridino association. Russian Geology
960 and Geophysics 53, 1023–1054.
961 Droop G.T.R., 1989. Reaction history of garnet-sapphirine granulites and conditions of
962 Archaean high-pressure granulite-facies metamorphism in the Central Limpopo
963 Mobile Belt, Zimbabwe. Journal of Metamorphic Geology 7, 383-403.
964 Dumond G., Goncalves P., Williams M.L., Jercinovic M.J., 2010. Subhorizontal fabric
965 in exhumed continental lower crust and implications for lower crustal flow:
966 Athabasca granulite terrane, western Canadian Shield, Tectonics 29, TC2006,
967 doi:10.1029/2009TC002514.
968 Eckert J.O., Newton R., Kleppa O., 1991. The ΔH of reaction and recalibration of
969 garnet – pyroxene – plagioclase – quartz geobarometers in the CMAS system by
970 solution calorimetry. American Mineralogist 76, 148-160.
971 Ellis D., Green D., 1979. An experimental study of the effect of Ca upon garnet-
972 clinopyroxene Fe-Mg exchange equilibria. Contributions to Mineralogy and
973 Petrology 71, 13-22.

974 Green E.C.R., White R.W., Diener J.F.A., Powell R., Holland T.J.B., Palin R.M., 2016.
975 Activity–composition relations for the calculation of partial melting equilibria in
976 metabasic rocks. Journal of Metamorphic Geology 34, 845-869.
977 Grimes C.B., John B.E., Kelemen P.B., Mazdab F.K., Wooden J.L., Cheadle M.J.,
978 Hanghøj K., Schwartz J.J., 2007. Trace element chemistry of zircons from oceanic
979 crust: A method for distinguishing detrital zircon provenance. Geology 35, 643–
980 646.
981 Gumsley A.P., 2017. Validating the existence of the supercraton Vaalbara in the
982 Mesoarchaean to Palaeoproterozoic. Doctoral dissertation, Lithosphere and
983 Biosphere Science, Department of Geology, Lund University. Litholund theses 30,
984 130.
985 Harley S.L., 1984. An experimental study of the partitioning of Fe and Mg between
986 garnet and orthopyroxene. Contributions to Mineralogy and Petrology 86, 359-373.
987 Harris L.B., Koyi H.A., Fossen H., 2002. Mechanisms for folding of high-grade rocks
988 in extensional tectonic settings. Earth-Science Reviews 59,163–210.
989 Herwartz D., Skublov S.G., Berezin A.V., Mel'nik A.E., 2012. First Lu-Hf garnet ages
990 of eclogites from the Belomorian mobile belt (Baltic Shield, Russia). Doklady
991 Earth Sciences 443, 377-380.
992 Holland T.J.B., Powell R., 1998. An internally consistent thermodynamic data set for
993 phases of petrological interest. Journal of Metamorphic Geology 16, 309–343.
994 Holland T.J.B., Powell R., 2011. An improved and extended internally consistent
995 thermodynamic dataset for phases of petrological interest, involving a new equation
996 of state for solids. Journal of Metamorphic Geology 29, 333–383.
997 Holland T.J.B., Powell R., 2003. Activity–composition relations for phases in
998 petrological calculations: an asymmetric multicomponent formulation. Contribution
999 to Mineralogy and Petrology 145, 492–501.

1000 Hoskin P.W., Black L.P., 2000. Metamorphic zircon formation by solid-state
1001 recrystallization of protolith igneous zircon. Journal of Metamorphic Geology 18,
1002 423–439.
1003 Iizuka T., Yamaguchi T., Itano K., Hibiya Y., Kazue Suzuki K., 2017. What Hf isotopes
1004 in zircon tell us about crust–mantle evolution. Lithos 274–275, 304–327.
1005 Imayama T., Oh C-W. Baltybaev S.K., Park C-S., Yi K., Jung H., 2017.
1006 Paleoproterozoic high-pressure metamorphic history of the Salma eclogite on the
1007 Kola Peninsula, Russia. Lithosphere 9, 855–873.
1008 Ingebritsen S.E., Manning C.E., 2002. Diffuse fluid flux through orogenic belts:
1009 Implications for the world ocean. PNAS 99, 9113-9116.
1010 Johnson T.E., Brown M., Gardiner N.J., Kirkland C.L., Smithies R.H.,2017. Earth's
1011 first stable continents did not form by subduction. Nature 543, 239-242.
1012 Jolivet L., Faccenna C., Goffe B., Burov E., Agard P., 2003. Subduction tectonics and
1013 exhumation of high-pressure metamorphic rocks in the Mediterranean orogens.
1014 American Journal of Science 303, 353-409.
1015 Kennedy A.K., de Laeter J.R., 1994. The performance characteristics of the WA
1016 SHRIMP II ion microprobe. In: Eighth International Conference on
1017 Geochronology, Cosmochronology and Isotope Geology. Berkeley, USA. Abstract
1018 Vol., U.S. Geological Survey Circular, 1107, 166.
1019 Komiya T, Maruyama S, Masuda T, Nohda S, Hayashi M, Okamoto K., 1999. Plate
1020 Tectonics at 3.8-3.7 Ga: Field evidence from the Isua accretionary complex,
1021 Southern West Greenland. Journal of Geology 107, 515-554.
1022 Komiya T., Yamamoto S., Aoki S., Sawaki Y., Ishikawa A., Tashiro T., Koshida K.,
1023 Shimojo, M, Aoki K., Collerson K.D., 2015. Geology of the Eoarchean, >3.95 Ga,
1024 Nulliak supracrustal rocks in the Saglek Block, northern Labrador, Canada: the
1025 oldest evidence for plate tectonics. Tectonophysics 662, 40-66.

1026 Krogh E.J., 1988. The garnet-clinopyroxene Fe-Mg geothermometer—a reinterpretation
1027 of existing experimental data. Contributions to Mineralogy and Petrology 99, 44-
1028 48.
1029 Kumar A., Parashuramulu V., Shankar R., Besse J., 2017. Evidence for a Neoarchean
1030 LIP in the Singhbhum craton, eastern India: Implications to Vaalbara
1031 supercontinent. Precambrian Research 292, 163–174.
1032 Kwan L.C.J., Zhao G., Yin C., Geng H., 2016. Metamorphic P-T path of mafic
1033 granulites from Eastern Hebei: Implications for the Neoarchean tectonics of the
1034 Eastern Block, North China Craton. Gondwana Research 37, 20-38.
1035 Li X., Zhang L., Wei C., Slabunov A.I., 2015. Metamorphic PT path and zircon U–Pb
1036 dating of Archean eclogite association in Gridino complex, Belomorian province,
1037 Russia. Precambrian Research 268, 74–96.
1038 Liu P., Liu F., Liu C., Wang F., Liu J., Yang H., Cai J., Shi J., 2013. Petrogenesis, P–T–
1039 t path, and tectonic significance of high-pressure mafic granulites from the Jiaobei
1040 terrane, North China Craton. Precambrian Research 233, 237–258.
1041 Liu S., Jahn B-M, Wan Y., Xie H., Wang S., Xie S., Dong C., Ma M., Liu D., 2015.
1042 Neoarchean to Paleoproterozoic high-pressure mafic granulite from the Jiaodong
1043 Terrane, North China Craton: Petrology, zircon age determination and geological
1044 implications. Gondwana Research 28, 493-508.
1045 Ludwig K.R., 2003. Isoplot 3.0. A Geochronological Toolkit for Microsoft Excel:
1046 Berkeley Geochron, Center Spec. Publ. vol. 4, 70 pp.
1047 Ludwig K.R., 2009. SQUID II., a user's manual, Berkeley Geochronology Center
1048 Special Publication 2, 2455 Ridge Road, Berkeley, CA 94709, USA 22.
1049 McDonough W.F., Sun S.-S., 1995. The composition of the Earth. Chemical Geology
1050 120, 223–253.

1051 Masquelin H., Lara H.S., Bettucci L.S., Demarco P.N., Pascual S., Muzio R., Peel El.,
1052 Scaglia F., 2017. Lithologies, structure and basement-cover relationships in the
1053 schist belt of the Dom Feliciano Belt in Uruguay. Brazilian Journal of Geology 47,
1054 21-42.
1055 Mel'nik A.E., Skublov S.G., Marin Y.B., Berezin A.V., Bogomolov E.S., 2013. New
1056 data on the age (U-Pb, Sm-Nd) of garnetites from Salma eclogites of the
1057 Belomorian mobile belt: Doklady Earth Sciences 448, 78–85.
1058 doi:10.1134/S1028334X13010133.
1059 Mello E. F., Xavier R. P., McNaughton N. J., Hagemann S. G., Fletcher I., Snee L.,
1060 2006. Age constraints on felsic intrusions, metamorphism and gold mineralization
1061 in the Paleoproterozoic Rio Itapicuru greenstone belt, NE Bahia State, Brazil.
1062 Mineralium Deposita 40, 849–866.
1063 Mints M.V., Belousova E.A., Konilov A.N., Natapov L.M., Shchipansky A.A., Griffin
1064 W.L., O'Reilly S.Y., Dokukina K.A., Kaulina T.V., 2010. Mesoarchean subduction
1065 processes: 2.87 Ga eclogites from the Kola Peninsula, Russia. Geology 38, 739–
1066 742.
1067 Mints M.V., Dokukina K.A., Konilov A.N., 2014. The Meso-Neoarchaean Belomorian
1068 eclogite province: Tectonic position and geodynamic evolution. Gondwana
1069 Research 25, 561–584.
1070 Möller A., O'Brien P.J., Kennedy A., Kröner A., 2002. Polyphase zircon in ultrahigh-
1071 temperature granulites (Rogaland, SW Norway): constraints for Pb diffusion in
1072 zircon. Journal of metamorphic Geology 20, 727–740.
1073 Morel M.L.A., Nebel O., Nebel-Jacobsen Y.J., Miller J.S., Vroon P.Z., 2008. Hafnium
1074 isotope characterization of the GJ-1 zircon reference material by solution and laser-
1075 ablation MC-ICPMS. Chemical Geology, 255, 231-235.

1076 Moser D.E., Flowers R.M., Hart R.J., 2001. Birth of the Kaapvaal tectosphere 3.08
1077 billion years ago. Science 291, 465–468.
1078 Moyen J-F., Stevens G., Kisters A., 2006. Record of mid-Archaean subduction from
1079 metamorphism in the Barberton terrane, South Africa. Nature 442, 559-562.
1080 Myers J., 1976. Granitoid sheets, thrusting, and crustal thickening in West Greenland.
1081 Geology 4, 265-268.
1082 Navarro M.S., Tonetto E.M., Oliveira E.P., 2015. LA-SF-ICP-MS U-Pb zircon dating at
1083 University of Campinas, Brazil. Geonalysis 2015, Vienna, Austria, P-09.
1084 Newton R., Perkins D., 1982. Thermodynamic calibration of geobarometers based on
1085 the assemblages garnet-plagioclase-orthopyroxene (clinopyroxene)-quartz.
1086 American Mineralogist 67, 203-222.
1087 O'Brien P.J., Rötzler J., 2003. High-pressure granulites: formation, recovery of peak
1088 conditions and implications for tectonics: Journal of Metamorphic Geology 21, 3-
1089 20.
1090 O'Neill J., Boyet M., Carlson R.W., Paquette J-L., 2013. Half a billion years of
1091 reworking of Hadean mafic crust to produce the Nuvvuagittuq Eoarchean felsic
1092 crust. Earth and Planetary Science Letters 379, 13-25.
1093 Oh C.W., Liou J.G., 1998. A petrogenetic grid for eclogite and related facies under
1094 high-pressure metamorphism. Island Arc 7, 36-51.
1095 Oliveira E. P., Souza Z. S., McNaughton N. J., Lafon J-M., Costa F. G., Figueiredo A.
1096 M., 2011. The Rio Capim volcanic-plutonic-sedimentary belt, São Francisco
1097 Craton, Brazil: Geological, geochemical and isotopic evidence for oceanic arc
1098 accretion during Palaeoproterozoic continental collision. Gondwana Research 19,
1099 735–750.
1100 Oliveira E.P, Amaral W., Baldim M.R., Talavera C., Sombini, G., Semprich, J.,
1101 McNaughton N., 2016. The Uauá microblock, northern S. Francisco Craton: a key

1102 area to understanding crustal growth during global spread of plate tectonics in the
1103 Mesoarchaean. 48th Brazilian Geological Congress, Porto Alegre, Brazil, Abstract
1104 8445.
1105 Oliveira E.P. 2011. The Late Archaean Uauá Mafic Dyke Swarm, São Francisco
1106 Craton, Brazil, and implications for Palaeoproteozoic extrusion tectonics and
1107 orogen reconstruction. In: Srivastava, R.K. (Ed) "Dyke Swarms: Keys for
1108 Geodynamic Interpretation". Springer, Berlin, p.19-31.
1109 Oliveira E.P. McNaughton N. J., Armstrong R. 2010. Mesoarchaean to
1110 Palaeoproterozoic growth of the northern segment of the Itabuna-Salvador-Curaçá
1111 orogen, São Francisco Craton, Brazil. In: Kusky, T. M., Zhai, M.-G. & Xiao, W.
1112 (Eds.) The Evolving Continents: Understanding Processes of Continental Growth.
1113 Geological Society, London, Special Publications 338, 263–286.
1114 Oliveira E.P., Mello E.F., McNaughton N., 2002. Reconnaissance U-Pb geochronology
1115 of early Precambrian quartzites from the Caldeirão belt and their basement, NE São
1116 Francisco Craton, Bahia, Brazil: Implications for the early evolution of the
1117 Palaeoproterozoic Salvador-Curaçá Orogen. Journal of South American Earth
1118 Sciences, 15: 349-362.
1119 Oliveira E.P., Silveira E.M., Söderlund U., Ernst R.E., 2013. U-Pb ages and
1120 geochemistry of mafic dyke swarms from the Uauá Block, São Francisco Craton,
1121 Brazil: LIPs remnants relevant for Late Archaean break-up of a supercraton. Lithos
1122 174, 308-322.
1123 Oliveira E.P., Souza Z.S., Corrêa Gomes L.C., 2000. U-Pb dating of deformed mafic
1124 dyke and host gneiss: Implications for understanding reworking processes on the
1125 western margin of the Archaean Uauá block, NE São Francisco Craton, Brazil.
1126 Brazilian Journal of Geology 30, 149-152.

1127 Oliveira E.P., Windley B.F., McNaughton N., Pimentel M., Fletcher I.R., 2004.
1128 Contrasting copper and chromium metallogenic evolution of terranes in the
1129 Palaeoproterozoic Itabuna-Salvador-Curaçá Orogen, São Francisco Craton, Brazil:
1130 new zircon (SHRIMP) and Sm-Nd (model) ages and their significance for orogen-
1131 parallel escape tectonics. Precambrian Research 128, 143-165.
1132 Paixão M.A.P., Oliveira E.P., 1998. The Lagoa da Vaca complex: an Archaean layered
1133 anorthosite body on the western edge of the Uauá block, Bahia, Brazil. Revista
1134 Brasileira de Geociencias 28, 201-208.
1135 Palin R.M., Weller O.M., Waters D.J., Dyck B., 2016. Quantifying geological
1136 uncertainty in metamorphic phase equilibria modelling; a Monte Carlo assessment
1137 and implications for tectonic interpretations. Geoscience Frontiers 7, 591–607.
1138 Paton C., Woodhead J.D., Hellstrom J.C., Hergt J.M., Greig A., Maas R., 2010.
1139 Improved laser ablation U–Pb zircon geochronology through robust downhole
1140 fractionation correction. Geochemical and Geophysical Geosystems 11(3),
1141 Q0AA06.
1142 Polat A., 2013. Geochemical variations in Archean volcanic rocks, southwestern
1143 Greenland: Traces of diverse tectonic settings in the early Earth. Geology 41, 379–
1144 380.
1145 Polat A., Kerrich R., Windley B.F. 2009. Archean crustal growth processes in southern
1146 West Greenland and the southern Superior Province: geodynamic and magmatic
1147 constraints. In: Earth Accretionary Systems in Space and Time. Cawood, P. A.,
1148 Kröner, A., (Eds.), Geological Society of London, Special Publications 318, 155-
1149 191.
1150 Powell R., 1985. Regression diagnostics and robust regression in
1151 geothermometer/geobarometer calibration: the garnet-clinopyroxene
1152 geothermometer revisited. Journal of Metamorphic Geology 3, 231-243.

1153 Powell1 R., Evans K.A., Green E.C.R., White R.W., 2018. On equilibrium in non-
1154 hydrostatic metamorphic systems. Journal of Metamorphic Geology 36, 419–438.
1155 Ravna K., 2000. The garnet-clinopyroxene Fe2+-Mg geothermometer: an updated
1156 calibration. Journal of Metamorphic Geology 18, 211-219.
1157 Reuber G., Kaus B.J.P., SchmalholzS.M., White R.W., 2016. Nonlithostatic pressure
1158 during subduction and collision and the formation of (ultra)high-pressure rocks.
1159 Geology 44, 343–346.
1160 Rubatto D., 2002. Zircon trace element geochemistry: partitioning with garnet and the
1161 link between U–Pb ages and metamorphism. Chemical Geology 184, 123–138.
1162 Saha L., Pant N.C., Pati J.K., Upadhyay D., Berndt J., Bhattacharya A., Satynarayanan
1163 M., 2011. Neoarchean high-pressure margarite–phengitic muscovite–chlorite
1164 corona mantled corundum in quartz-free high-Mg, Al phlogopite–chlorite schists
1165 from the Bundelkhand craton, north central India. Contribution to Mineralogy and
1166 Petrology 161, 511–530.
1167 Sajeev K., Santosh M., 2006. Extreme crustal metamorphism and crust-mantle
1168 processes: an introduction. Lithos 92, v-ix.
1169 Sajeev K., Windley B.F., Connolly J.A.D., Kon Y., 2009. Retrogressed eclogite (20
1170 kbar, 1020°C) from the Neoproterozoic Palghat-Cauvery suture zone, southern
1171 India. Precambrian Research 171, 23-36.
1172 Sajeev K., Windley B.F., Hegner E., Komiya T., 2013. High-temperature, high-pressure
1173 granulites (retrogressed eclogites) in the central region of the Lewisian, NW
1174 Scotland: Crustal-scale subduction in the Neoarchaean. Gondwana Research 23,
1175 526–538.
1176 Salminen J., Oliveira E.P., Piispa E.J., Smirnov A.V., Trindade R.I.F., 2018. Revisiting
1177 the paleomagnetism of the Neoarchean Uauá mafic dyke swarm Brazil:
1178 Implications for Archean supercratons. Precambrian Research.

https://doi.org/10.1016/j.precamres.2018.12.001

Samuel V.O., Sajeev K., Hokada T., Horie K., Itaya T., 2015. Neoarchean arc magmatism followed by high-temperature, high-pressure metamorphism in the Nilgiri Block, southern India. Tectonophysics 662, 109-124.

Schamalholz S., Podladchikov Y., 2014. Metamorphism under stress: The problem of relating minerals to depth. Geology 42, 733–734.

Shirey S.B., Richardson S.H., 2011. Start of the Wilson Cycle at 3 Ga shown by diamonds from subcontinental mantle. Science 333, 434-436.

Sizova E., Gerya T., Stüwe K, Brown M., 2015. Generation of felsic crust in the Archean: A geodynamic modeling perspective. Precambrian Research 271, 198–224.

Skublov S.G., Balashov Y.A., Marin Y.B., Berezin A.V., Mel'nik A.E., and Paderin I.P., 2010. U-Pb age and geochemistry of zircons from Salma eclogites (Kuru-Vaara deposit, Belo- morian Belt): Doklady Earth Sciences 432, 791–798, doi:10.1134/S1028334X10060188.

Skublov S.G., Berezin A.V., Mel'nik A.E., 2011. Paleoproterozoic eclogites in the Salma area, northwestern Belomorian mobile belt: Composition and isotopic geochronologic characteristics of minerals and metamorphic age: Petrology 19, 470–495. doi:10.1134/S0869591111050055.

Smirnov A.V., Evans, D.A.D,. Ernest R.E, Söderlund U., Li, Z.X., 2013. Trading partners: Tectonic ancestry of southern Africa and western Australia, in Archean supercratons Vaalbara and Zimgarn. Precambrian Research. 224: pp. 11-22.

Spear F., Kohn M., Florence F., Menard T., 1990. A model for garnet and plagioclase growth in pelitic schists: implications for thermobarometry and P-T path determinations. Journal of Metamorphic Geology 8, 683-696.

1205 Spear F.S., Selverstone J., 1983. Quantitative PT paths from zoned minerals: theory and
1206 tectonic applications. Contributions to Mineralogy and Petrology 83, 348-357.
1207 Stern R.S., 2001. A new isotopic and trace-element standard for the ion microprobe:
1208 preliminary thermal ionization mass spectrometry (TIMS) U-Pb and electron-
1209 microprobe data. Geological Survey of Canada. Current Research 2001-F1. (page
1210 numbers?)
1211 Stern R.S., Bodorkos S., Kamo S. L., Hickman A. H., Corfu F., 2009. Measurement of
1212 SIMS instrumental mass fractionation of Pb-isotopes during zircon dating.
1213 Geostandards and Geoanalytical Research, 33, 145-168.
1214 Tajcmanová L., 2015. Deviations from lithostatic pressure during metamorphism:
1215 fact or fiction? Jounal of metamorphic Geology 33, 783–784.
1216 Tang M., Chen K., Rudnick R.L., 2016. Archean upper crust transition from mafic to
1217 felsic marks the onset of plate tectonics. Science 351, 372-375.
1218 Teixeira W., Oliveira E.P., Marques L.S., 2017. Nature and evolution of the Archean
1219 crust of the São Francisco Craton. In: M. Heilbron et al. (Eds.), São Francisco
1220 Craton, Eastern Brazil, Springer, Switzerland, Regional Geology Reviews, pp.
1221 29-56.
1222 Van Kranendonk M.J., Smithies R.H., Hickman A.H., Champion D.C., 2007. Secular
1223 tectonic evolution of Archean continental crust: interplay between horizontal and
1224 vertical processes in the formation of the Pilbara Craton, Australia. Terra Nova 19,
1225 1–38.
1226 Van Reenen D.D., Barton Jr. J.M., Roering C., Smith C.A., Van Schalkwyk J.F., 1987.
1227 Deep crustal response to continental collision; The Limpopo belt of southern
1228 Africa. Geology 15, 11-14.
1229 Vavra G., Gebauer D., Schmid R., Compston W., 1996. Multiple zircon growth and
1230 recrystallization during polyphase Late Carboniferous to Triassic metamorphism in

granulites of the Ivrea Zone (Southern Alps): an ion microprobe (SHRIMP) study. Contributions to Mineralogy and Petrology 122, 337–358.

Vendemiatto M.A., Enzweiler J., 2001. Routine control of accuracy in silicate rock analysis by X-ray fluorescence spectrometry. Geostandards Newsletter-The Journal of Geostandards and Geoanalysis 25, 283–291.

Verma S.K., Verma S.P., Oliveira E.P., Singh V.K., Moreno J.A., 2016. LA-SF-ICP-MS zircon U–Pb geochronology of granitic rocks from the central Bundelkhand greenstone complex, Bundelkhand craton, India Journal of Asian Earth Sciences 118, 125–137.

Volodichev O.I., Slabunov A.I., Bibikova E.V., Konilov A.N., Kuzenko T.I., 2004. Archean eclogites in the Belomorian Mobile Belt, Baltic Shield. Petrology 12, 540–560.

Wang D., Guo J., 2017. Late Archean high-pressure pelitic granulites in the Yinshan Block, North China Craton Precambrian Research 303, 251-267.

Wei C. J., Zhang C. G., Zhang A. L., Wu T. H., Li J. H., 2001. Metamorphic P-T conditions and geological significance of high-pressure granulite from the Jianping complex, western Liaoning province. Acta Petrologica Sinica 17, 269–282.

Wheeler J., 2014. Dramatic effects of stress on metamorphic reactions. Geology 42, 647–650.

White R.W., Powell R., Holland T.J.B., Johnson T.E., Green E.C.R., 2014. New mineral activity–composition relations for thermodynamic calculations in metapelitic systems. Journal of Metamorphic Geology 32, 261–286.

White R.W., Powell R., Holland T.J.B., Worley B.A., 2000. The effect of TiO2 and Fe2O3 on metapelitic assemblages at greenschist and amphibolite facies conditions: mineral equilibria calculations in the system K2O–FeO–MgO–Al2O3–SiO2–H2O–TiO2–Fe2O3. Journal of Metamorphic Geology 18, 497–511.

1257 Wiedenbeck M., Allé P., Corfu F., Griffin W.L., Meier M., Oberli F., Von Q.A.,
1258 Roddick J.C., Spiegel W., 1995. Three natural zircon standards for U–Th–Pb, Lu–
1259 Hf, trace element and REE analyses. Geostandards Newsletter 19, 1–23.
1260 Williams M.L., Karlstrom K.E., Dumond G., Mahan K.H., 2009. Perspectives on the
1261 architecture of continental crust from integrated field studies of exposed isobaric
1262 sections. Geological Society of America, Special Paper 456, 219-241.
1263 Windley B.F., Garde A.A., 2009. Arc-generated blocks with crustal sections in the
1264 North Atlantic craton of West Greenland: crustal growth in the Archean with
1265 modern analogues. Earth-Science Reviews 93, 1-30.
1266 Windley B.F., 1995. The evolving continents. John Wiley & Sons Ltd. 3rd Edition.
1267 Yu H., Zhang L., Lanari P., Rubatto D., Li X., 2019. Garnet Lu-Hf geochronology and
1268 P-T path of the Gridino-type eclogite in the Belomorian Province, Russia. Lithos
1269 326–327, 313–326.